공학석사 학위논문

자기유도형 무선전력전송 시스템의 효과적인 동적 부하 추정

Effective Dynamic Load Identification for Inductive Wireless Power Transfer Systems

울산대학교 대학원

전기전자컴퓨터공학과

ANDREW NGINI MWANGI

공학석사 학위논문

자기유도형 무선전력전송 시스템의 효과적인 동적 부하 추정

Effective Dynamic Load Identification for Inductive Wireless Power Transfer Systems

지도교수 최성진

이 논문을 공학석사 학위논문으로 제출함

2025 년 12 월

울산대학교 대학원

전기전자컴퓨터공학과

ANDREW NGINI MWANGI

ANDREW NGINI MWANGI 의

공학석사학위 논문을 인준함.

심사위원장	손영광	(인)
심사위원	최성진	(인)
심사위원	서영수	(인)

울산대학교 대학원

전기전자컴퓨터공학과

2025 년 12 월

UNIVERSITY OF ULSAN

Effective Dynamic Load Identification for Inductive Wireless Power Transfer Systems

by

ANDREW NGINI MWANGI

Supervisor: Professor SUNG-JIN CHOI

A dissertation submitted in partial fulfillment of

the requirements for the degree of Master of Science

in the

Department of Electrical, Electronic and Computer Engineering

University of Ulsan

December 2025

This certifies that the dissertation of ANDREW NGINI MWANGI

is approved by:

Committee Chair: **Professor Young-Kwang Son**

Signature:

Committee Member: **Professor Sung-Jin Choi**

Signature:

Committee Member: **Professor Young-Soo Suh**

Signature:

Department of Electrical, Electronic, and Computer Engineering

University of Ulsan

December 2025

I would like to dedicate this thesis to my loving parents and siblings.

Acknowledgements

I would like to express my heartfelt gratitude to my academic advisor, Professor Sung-Jin Choi, for his expert supervision, thoughtful discussions, and technical insight, which were essential during my Master's degree at the University of Ulsan. It is such an honor to be one of his power electronics graduate students.

I would like to express my sincere thanks to Professor Young-Kwang Son, and Professor Young-Soo Suh for serving as members of my thesis committee. Your valuable comments and suggestions greatly helped improve the quality of my thesis.

I would like to also express my gratitude to Brain Korea 21 Plus (BK21+) and the National Research Foundation of Korea (NRF) for their support in my pursuit of this Master's degree.

I would also like to extend my appreciation to the lab members of the Energy Conversion and Circuit Laboratory (ECCL) for their helpful discussions, collaborations, and the many memorable moments shared.

Finally, to my family and friends, I am deeply thankful for the encouragement during this academic journey.

Andrew Ngini Mwangi
Ulsan, South Korea
December 2025

국문 요약

자기유도형 무선전력전송 시스템의 효과적인 동적 부하 추정

울산대학교 대학원
전기전자컴퓨터공학과
꽝기 앤드류 능기니

자기유도형 무선전력전송(Inductive Wireless Power Transfer, IWPT) 기술은 소형 가전제품부터 전기자동차 및 선박에 이르기까지 다양한 응용 분야에서 전력을 전달하기 위한 편리하고 비접촉식의 수단으로 빠르게 발전하고 있다. 최근 IWPT 시스템은 수신기(2차 측)에서의 피드백 경로를 이용하던 기존 방식에서 벗어나, 송신기(1차 측)에서 수신기 측 출력 매개변수를 직접 식별하는 방식으로 발전하고 있다. 이러한 IWPT 시스템의 설계 및 1차 측 제어에서의 핵심 과제는 시스템 내 전력 전달 특성에 직접적인 영향을 미치는 2차 측 매개변수, 특히 부하저항, 출력전류 및 전압을 정확하게 식별하는 것이다.

수신기에서 송신기로의 통신 채널을 제거하여 측정 피드백을 전달하지 않는 실용적 시스템에서는, 비용과 복잡성을 최소화하기 위해 1차 측 전압 및 전류 측정값만을 이용하여 매개변수를 식별해야 한다. 그러나 이러한 1차 측 측정값은 취득 과정에서 측정 오차 및 프로세스 오차에 의해 왜곡되며,

해석적인 수식 기반의 기존 식별 기법은 이러한 노이즈를 그대로 전파하거나 증폭시키는 경향이 있다. 또한, 다른 기존의 기법들은 시스템의 정상적인 전력 전송을 방해하거나 추가적인 하드웨어 구현을 요구하는 등의 한계가 있다. 이러한 제약으로 인해, 노이즈와 부하 변화에 강인하면서도 비침입적이고 실시간으로 동작 가능한 1 차 측 식별 기법의 필요성이 대두되고 있다.

본 논문에서는 이러한 문제를 해결하기 위하여, 실용적인 1차 측 식별 전략을 개발하고 이를 실험적으로 검증하였다. 제안된 방법은 첫 번째 단계에서 출력 부하저항을 기초 매개변수로 해석적으로 식별하고, 두 번째 단계에서는 식별된 저항 값을 기반으로 시스템의 상태공간 칼만 필터 모델을 도출하여 출력 부하전압을 추정한다. 본 1 단계 식별 전략은 시스템의 전력 전송을 방해하지 않으면서 선형 추정기를 통해 비선형 시스템을 분리하므로, 노이즈 및 부하 변동 환경에 강인한 추정이 가능하다는 장점을 가진다. 또한, 제안된 식별 기법의 오프 공진 동작 조건에서의 성능을 관찰하기 위해, 1차 측 전압과 전류 사이의 위상각 변화를 생성하는 디지털 위상 검출기 기반의 유한상태기계를 구현하였다. 제안된 식별 기법의 성능은 75 W 급 IWPT 하드웨어 테스트벤치를 이용한 시뮬레이션 및 실험을 통해 검증되었으며, 동적 운전 조건에서 최대 부하 변동 구간에서 추정 오차를 약 32%까지 감소시킴으로써 그 효용성을 입증하였다.

Effective Dynamic Load Identification for Inductive Wireless Power Transfer Systems

Andrew Ngini Mwangi
Dept. of Electrical, Electronic
And Computer Engineering,
The Graduate School,
University of Ulsan
Supervised by Prof. Sung-Jin Choi

ABSTRACT

Inductive wireless power transfer (IWPT) is rapidly developing as a convenient, contactless means of delivering power across applications such as small-scale consumer electronics to large-scale electric vehicles and vessels. Progressively, IWPT systems have migrated from the use of a feedback path from the secondary-side to the use of primary-side identification of the secondary-side output parameters. A central challenge in this IWPT design and its primary-side control is the accurate identification of secondary-side parameters, notably load resistance, output load current and voltage, as these parameters affect power transfer in the system. In a practical system that eliminates the communication channel of the feedback of its measurements from the receiver to the transmitter, parameter identification is performed from the

primary-side quantity measurements alone in order to keep the cost and complexity low. Unfortunately, primary-side voltage and current measurements are corrupted by measurement and process noise during acquisition, and purely analytical-based conventional identification methods tend to propagate and amplify these noise. Likewise, other conventional alternatives either disrupt power transfer operation in the system or require extra hardware implementation. These limitations create a necessity for a non-disruptive, real-time primary-side identification strategy that handles noise and dynamic load changes.

This thesis, therefore, aims to develop and experimentally validate a practical two-step primary-side identification strategy. First, the output load resistance is recognized analytically as a baseline parameter. Then, based on the recognized resistance parameter, a state-space dynamic Kalman model of the system is derived to track the output load voltage as the second step. This two-step identification strategy has the advantage of robust estimation in the presence of noise and load variations as it decouples the nonlinear system via a linear estimator without disrupting normal power transfer in the system. Also, in order to observe performance of the proposed identification strategy under off-resonance operation scenarios, a digital phase detector finite state machine is implemented to produce the phase angle change between the primary-side voltage and current. The efficacy of the proposed identification approach is confirmed through simulation and experimental validation using a 75 W IWPT hardware test-bench. Under dynamic operation, the proposed two-step identification approach reduces the estimation error by 32 % at maximum variation range.

Table of contents

List of figures

List of tables

Chapter 1

Introduction

1.1 Background of WPT Systems Technology

Wireless power transfer (WPT) technology has become increasingly prevalent in today's modern world. The advancement of this technology has primarily been facilitated by both near-field and far-field power transfer techniques, which have been optimized to enhance power transfer efficiency while addressing the fundamental limitations posed by various operating conditions. Near-field techniques, in particular inductive coupling, have exhibited significant strides in commercial viability. Applications range from small gadgets such as wrist watches to large vessels such as electric vehicles (EVs) [1], [2]. However, inherent restrictions, namely limited charging range and misalignment, present challenges to the power transfer process. The charging range in this case is the distance between the transmitting coupler and the receiving coupler in the system, and as the coupler distance increases, the energy transferring field depreciates along with the declination of power delivered to the load. Similar hypothesis is made for misalignment where imprecise alignment of transmitter and receiver affects the transferred power.

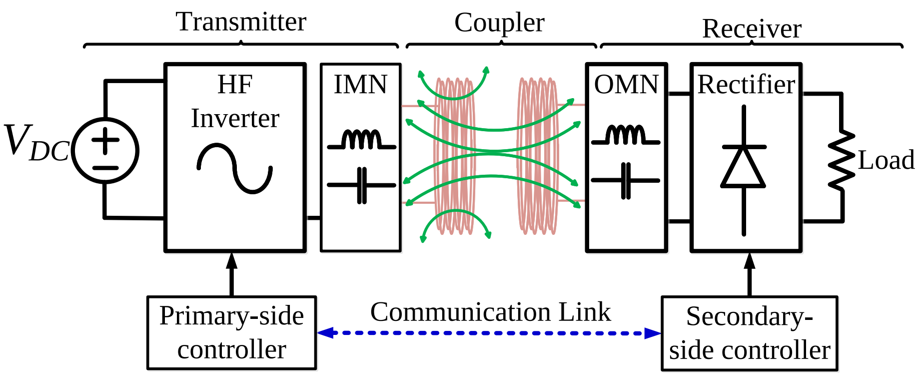

Fig. 1.1 Overall view of IWPT system.

Inductive wireless power transfer (IWPT) system is used as the main scope of reference since it is well established and widely used. In these systems, an alternating current (AC) from an inverter flows through a primary-side coil, generating a magnetic field in line with electromagnetic principles. This magnetic field in turn induces a voltage in the nearby secondary-side coil. The induced AC is then converted back to direct current (DC), thereby transferring energy without any physical connection to power devices as depicted in Fig. 1.1 where the compensation circuitry is represented as input matching network (IMN) and output matching network (OMN).

Under diverse operating conditions, the mutual inductance coupling between the primary-side coupler and secondary-side coupler, and the load varies, thereby influencing the power delivery quality. To regulate the power flow under these varying conditions, control system is essential. Conventionally, this is achieved by measuring output parameters on the receiver side and transmitting this data back to the primary side via a communication link or feedback path. This introduces latency, reliability issues due to signal interference, increased hardware costs, and system complexity. Consequently, there is a growing shift toward primary-side control strategies that do not use feedback from the secondary-side of the system.

1.2 Objectives of the Thesis

The aforementioned challenges of eliminating feedback path necessitates identification of secondary-side parameters solely through primary-side parameter measurements. However, achieving high accuracy in parameter identification is difficult because primary-side measurements are inevitably corrupted by sensing noise, and purely analytical mathematical models often propagate this noise, leading to amplified estimation errors. Therefore, the main motivation of the research carried out in this thesis stems from the limitations that have been surveyed and observed in conventional parameter identification techniques for IWPT systems. Following identified limitation associated with analytical-based methods that offer simplicity, on the other hand they suffer significantly from noise propagation, where measurement errors in primary-side sensors escalate into large deviations in subsequent estimated output parameters. To curb this, an effective identification technique is developed for a dynamic IWPT system. The objectives of this thesis are as follows:

A. Noise sensitivity analysis of conventional analytical method

This involves investigating how sensor noise variances propagate through circuit equations to degrade the accuracy of load resistance and subsequent output voltage estimation, establishing a clear motivation for a more effective noise handling-capable approach. The goal is to mathematically model and demonstrate the impact of noise propagation through conventional sole-analytical identification techniques where subsequent estimation is performed during system dynamic operation.

B. Effective identification structure

This objective is to formulate a communication-less identification algorithm that decouples the non-linear IWPT system into two manageable steps. This involves first establishing an analytical baseline for the equivalent load resistance and then designing a linear dynamic state-space model integrated with a Kalman filter estimator. The goal is to develop an estimator that can track the output load voltage parameter in dynamic load variations with improved accuracy while effectively handling measurement and model noise, without disrupting system operation.

1.3 Contributions of the Thesis

In this thesis, theoretical analysis, simulations and hardware testbench implementations for verification purposes have been carried out following the laid down objectives. Therefore, the main contributions of this thesis include:

• An extensive literature survey of the various existing primary-side identification methods. These are discussed and classified in accordance to the principles of operations. These classified categories include: analytical techniques, signal processing techniques, frequency sweeping techniques, impedance characteristic-based techniques and auxiliary circuit-based techniques.

• Proposal of a two-step identification method that combines the simplicity of analytical implementation with the noise handling capability and dynamicity of Kalman estimator. Unlike conventional methods that rely on a sole-analytical based approach which is prone to error propagation, this thesis utilizes the analytically obtained AC resistance from first step as a baseline input for a second step linear Kalman filter. This decoupling allows the approach to linearize the non-linear dynamics of the IWPT system prior, enabling improved tracking of the output load voltage parameter.

• To ensure the system performs correctly across different operating scenarios, this work develops a practical digital phase detector Finite-State-Machine (FSM). This module allows the system to detect the phase difference between primary voltage and current, facilitating parameter identification not only at resonance but also under detuned conditions with inductive or capacitive reflected impedances. This expands the applicability of the two-step identification method to practical scenarios where perfect system operation is not maintained.

• Since the proposed two-step identification method is implemented based only on the primary-side quantities of voltage and current, the system is uninterrupted during operation. Compared to conventional methods, such as frequency sweeping techniques, that require termination of normal system operation to perform identification, this merit enables the proposed method to be applicable in both static and dynamic charging cases.

1.4 Outline of the Thesis

Chapter 1 Introduction of the background of IWPT technology is shown where the need for eliminating feedback channels as well as establishing primary-side identification techniques are presented. In addition, limitations of conventional primary-side identifications are introduced. Furthermore, the objectives of this work together with the contributions that have been achieved in this thesis are outlined.

Chapter 2 The overview of IWPT system operation is described based on a series-series compensated IWPT system. An extensive literature survey on primary-side parameter identification in communication-less IWPT systems is presented. The study is done by classifying the numerous methods under an umbrella of five techniques.

Chapter 3 Conventional analytical identification method as the first step is discussed in this chapter. Firstly, analysis of the limitations associated with conventional sole-analytical identification approaches for subsequent parameter estimation is given. Then, the noise propagation impact of the sole-analytical identification is shown. This is demonstrated via system simulation for subsequent estimation of equivalent load resistance and output load voltage following analytical technique.

Chapter 4 An effective load identification approach for primary-side estimation is presented in this chapter. Analysis and modelling of the dynamic state-space linear discrete IWPT system is carried out. The linear Kalman estimator which is the second step of the two-step identification approach is utilized. A digital phase detector FSM for off-resonance system operation is designed and implemented.

Chapter 5 Validation of the proposed identification approach is performed through simulation and experiment. A hardware testbench setup is described in detail. Comparative experimental outcomes for nominal tuned and detuned system cases are presented.

Chapter 6 Conclusion of the work presented in this thesis is given as well as promising scopes of future research related to this thesis.

Chapter 2

Identification in Communication-less IWPT Systems

The purpose of the shifting focus to implementation of primary-side parameter identification methods is related to the goal of control methods to regulate the power in IWPT systems. A controller, particularly implemented on the primary-side, has conventionally been applied where parameters such as load voltage are fed back from secondary-side to primary-side controller via wireless communication channels. However, delay, high cost and complexity of the system are limitations that are associated with this implementation. Necessity for further innovation in primary-side control mechanisms that do not rely on any communication are crucial for maximizing the adaptability of these wireless systems across both static and dynamic applications [3]. Here 'static' pertains to the power transfer when transmitter and receiver couplers are in still position hence coupling condition is constant while 'dynamic' is where the position of the couplers vary.

In literature, [4] as well as [5] have proposed single controller for the IWPT system that required to only monitor and utilize parameters on the transmitting side of the system. [6], [7] have also highlighted the importance of developing techniques for primary-side parameter identification, which can adapt to the conditions of operation, thereby enhancing the overall efficiency and viability of wireless power transfer systems, especially when traditional communication methods are impractical or infeasible.

With the goal of simplicity and low cost of the system, front-end identification methods stand out as innovative solutions that address this challenge in IWPT systems as they play a role of acquiring information of system parameters to be utilized by the primary-side controller [8]. However, the trade-off between simplicity and accuracy remains a critical consideration [9]. Approaches leveraging experimentally obtained system parameters and advanced analysis techniques have been proposed, allowing for online and offline optimizations and performance evaluations under a wide range of operational scenarios [10]. Moreover, these methodologies not only enhance the efficiency of power transfer but also enable more adaptable control systems, leading to reduced reliance on cumbersome protocols associated with traditional charging systems, thereby addressing significant challenges of complexity observed in previous iterations of IWPT technologies [11].

In a general way, control strategies are broken down into double-side control, secondary-side control and primary-side control, with the goal of handling misalignment condition that occurs in the system. Misalignment may occur in both static and dynamic applications [12]. In double-side control strategy depicted in Fig. 2.1, both the primary-side and secondary-side of the wireless power system are tasked with the roles of control mechanisms to optimize power transfer efficiency, regulate output power, and ensure safe operation [13]. Conventionally, this

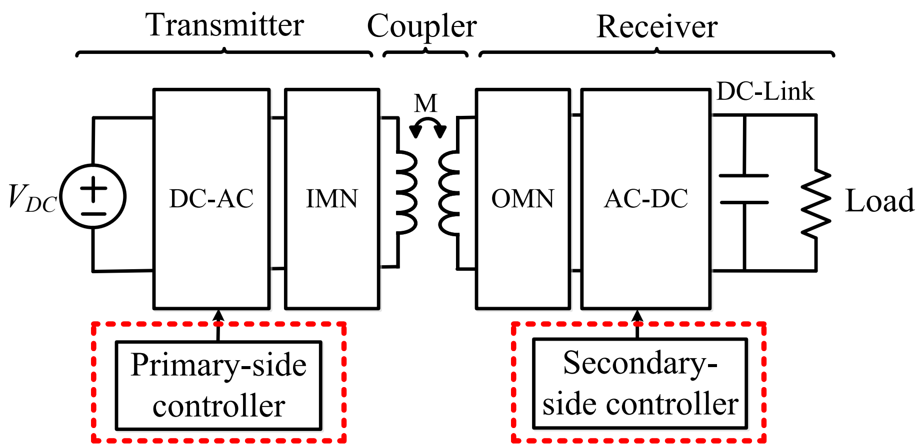

Fig. 2.1 Double-side control of IWPT.

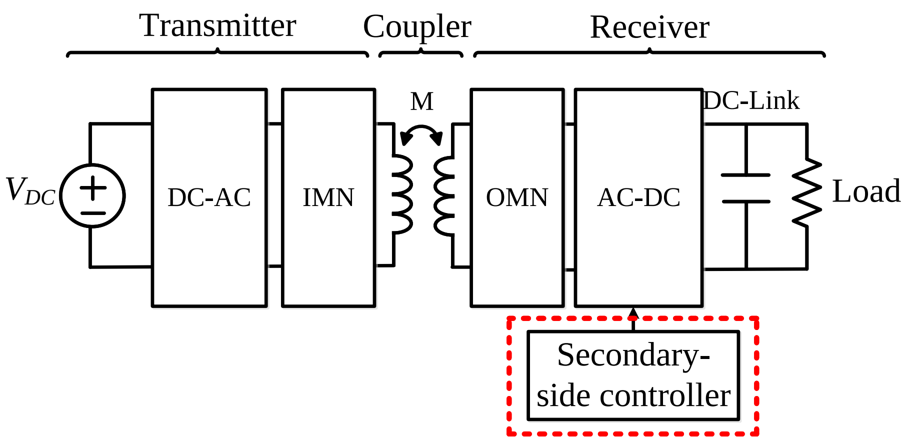

Fig. 2.2 Secondary-side control of IWPT.

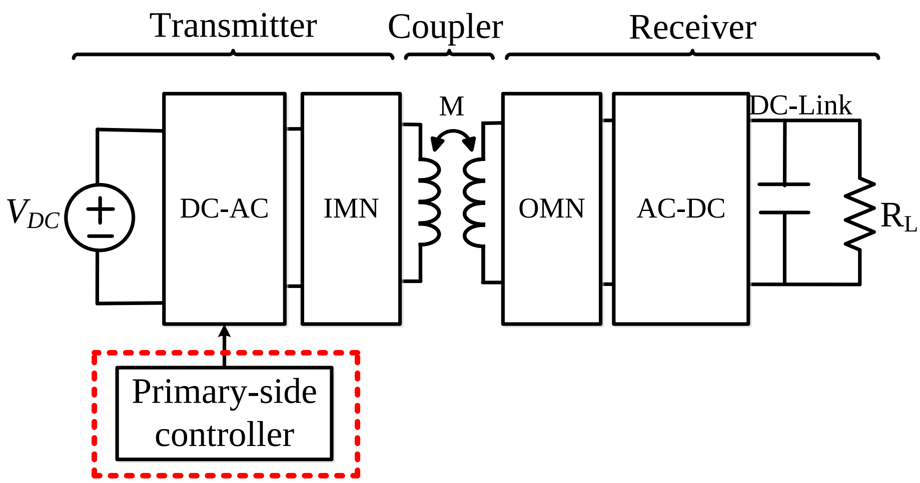

Fig. 2.3 Primary-side control of IWPT.

strategy is applied in systems where dynamic conditions affect the power transfer process [14]. Secondary-side control shown in Fig. 2.2 is associated with regulation and management of power on the receiving side of the IWPT system [15], [16]. This control is implemented for ensuring that the transferred power meets the required levels for charging or powering the load devices, maintaining efficiency, and protecting against overcharging or overheating of the system whereas primary-side control, as illustrated in Fig. 2.3, refers to the method of regulating the power transfer from the transmitting side to the receiving side of the system [17], [18]. This is achieved by either having a dedicated communication channel for feedback information or indirect parameter identification system parameters without using a feedback communication channel.

One of the essential tasks in primary-side control is the estimation of the aforementioned system parameters to be applied for various control methods [19]. Primary-side control without any wireless communication channel from the secondary-side approach is key for decreasing complexity and therefore cost of the IWPT system by having eliminated the receiving side's need for control along with communication hardware, particularly, in applications like electric vehicle (EV) charging, medical implants, and consumer electronics [20].

2.1 IWPT Operation

For the purpose of IWPT system analysis, this work will utilize the series-series (SS) compensated topology as illustrated in Fig. 2.4. In the equivalent circuit model of a two-coil SS-compensated IWPT system shown in Fig. 2.5, M is the mutual inductance coupling that quantifies the interaction between the primary-side and secondary-side coils. This M value can be expressed as

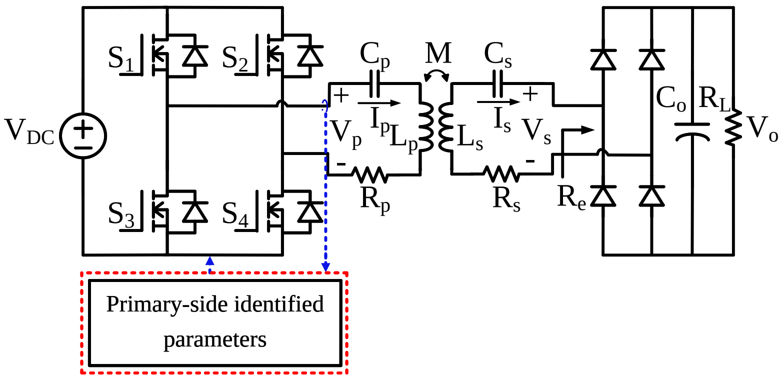

Fig. 2.4 Circuit diagram of a two-coil SS-compensated IWPT system with full-bridge inverter.

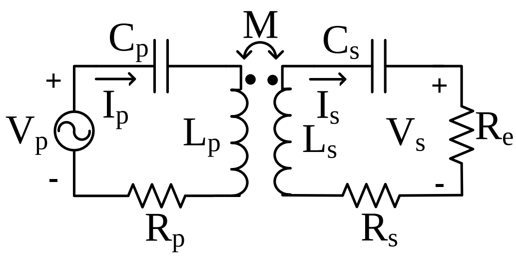

Fig. 2.5 Equivalent circuit model of a two-coil SS-compensated IWPT system.

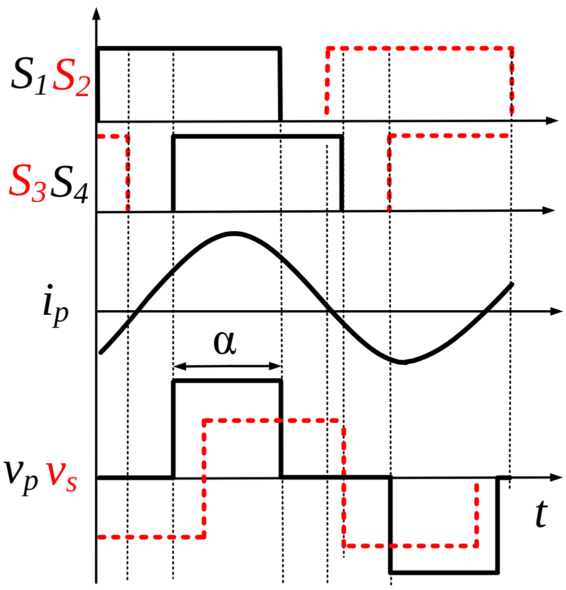

Fig. 2.6 Typical operational waveform of a phase-shifted full-bridge inverter on the primary-side.

$$M = k\sqrt{L_p L_s} \tag{2.1}$$

where k, L_p and L_s are coupling coefficient, primary-side self-inductance and secondary-side self-inductance, respectively. Considering the fundamental components of the voltage and current, the following analysis utilizing the Kirchhoff's voltage law can be performed to derive

$$\begin{bmatrix} v_{p1} \\ 0 \end{bmatrix} = \begin{bmatrix} j\omega L_p + \frac{1}{j\omega C_p} + R_p & j\omega M \\ j\omega M & j\omega L_s + \frac{1}{j\omega C_s} + R_s + R_e \end{bmatrix} \begin{bmatrix} i_{p1} \\ i_{s1} \end{bmatrix} \tag{2.2}$$

where ω is the operating angular frequency while R_p, R_s and R_e refer to the equivalent series resistances (ESR) of the transmitting side, receiving sides and the load equivalent resistance, respectively. Let impedances $j\omega L_p + \frac{1}{j\omega C_p} + R_p = Z_a$ and $j\omega L_s + \frac{1}{j\omega C_s} + R_s + R_e = Z_b$. In IWPT system cases where the load resistance R_L is used to represent a battery equivalent resistance for example in EV charging, then R_e and V_s of the rectifier, and output current I_o are inferred as

$$R_e = \frac{8}{\pi^2} R_L, V_s = \frac{2\sqrt{2}}{\pi} V_o, I_o = \frac{2\sqrt{2}}{\pi} I_s. \tag{2.3}$$

The V_p voltage produced from the full-bridge inverter is a square wave due to phase-shifted control signals to the switches S_1, S_2, S_3 and S_4 as illustrated in Fig. 2.6. Since only the fundamental component is considered at the primary compensation, the amplitude of the fundamental component, V_{p1}, of the equivalent circuit model in Fig. 2.5 is given as

$$V_{p1} = \frac{4V_{DC}}{\pi} \sin\left(\frac{\alpha}{2}\right) \sin(\omega t) \tag{2.4}$$

where V_{DC} is the system input DC voltage into the inverter and α is the conduction angle in consistent with the signals of the full-bridge switches. Looking at (2.2), equivalent input impedance seen from the full-bridge inverter is derived and obtained as

$$Z_{in} = \frac{V_p(s)}{I_p(s)} = R_{in} + j\mathrm{X}_{in} \tag{2.5}$$

where I_P is the primary-side current and

$$R_{in} = R_p + \frac{\omega^2 M^2 (R_e + R_s)}{(R_e + R_s)^2 + (\omega L_s - \frac{1}{\omega C_s})^2} \tag{2.6}$$

$$X_{in} = \omega L_p - \frac{1}{\omega C_p} - \frac{\left(\omega L_s - \frac{1}{\omega C_s}\right)\omega^2 M}{(R_e + R_s)^2 + (\omega L_s - \frac{1}{\omega C_s})^2}. \tag{2.7}$$

At resonance, the inductive reactance ωL and capacitive reactance $\frac{1}{\omega C}$ cancel each other out, hence leaving only the resistive component. This condition is desirable as it allows the compensation network to operate at maximum efficiency, in addition to minimal energy loss due to impedance. Managing the impedance to be slightly above resonant frequency is crucial for the system especially under varying conditions.

From here on, different assumptions and techniques are brought into use. Some works in literature assume that parasitic resistors R_p and R_s equal to zero, some assume the mutual inductance M does not change during system operation. Some works consider all the factors and the change of the mutual inductance M. Various parameter identification methods are now presented in the next section.

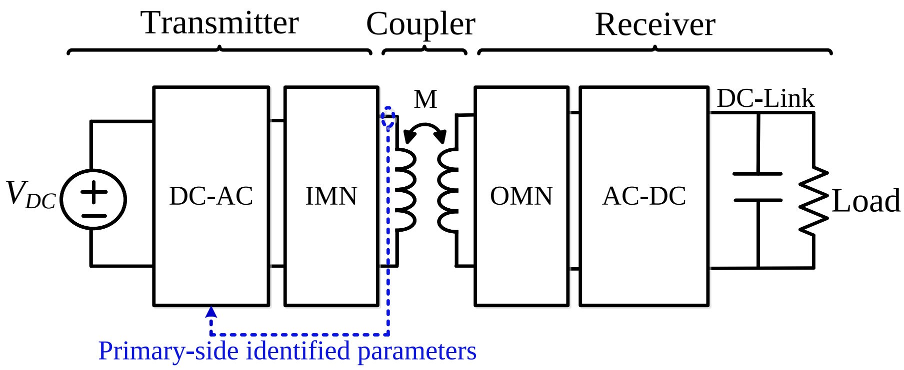

Fig. 2.7 Primary-side identification of system parameters.

Table 2.1 List of general system parameters.

Symbol	Parameters	Status
I_p	Primary side current	◯
V_p	Primary side voltage	◯
M	Mutual inductance	□
R_L	Load resistance	△
k	Coupling coefficient	□
V_o	Output voltage	△
I_o	Output current	△
f_p	Primary side resonant frequency	◯
f_s	Secondary side resonant frequency	□

Note: ◯ = Known, △ = Unkown, □ = Sometimes known

2.2 Identification in Communication-less IWPT Systems

Primary-side parameter estimation techniques are pursued with the effort to do away with a dedicated communication channel or feedback between the secondary-side and the primary-side of the IWPT system. This endeavor is accomplished by having the secondary-side observer implemented onto the primary-side of the system based solely on the primary-side parameter measurements as demonstrated in Fig. 2.7. In a typical identification process, data from known values of primary-side current or voltage or both is obtained either via

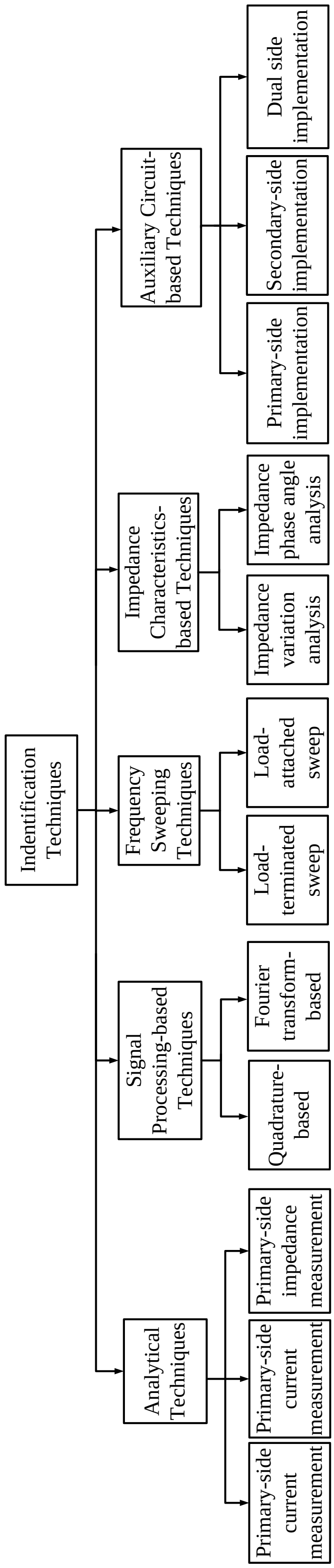

Fig. 2.8 Classification of primary-side identification techniques.

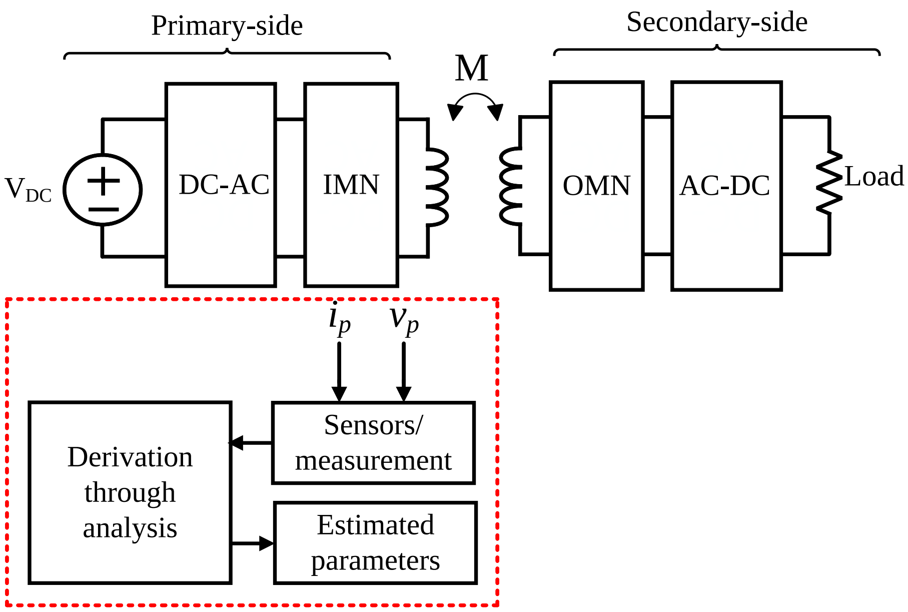

Fig. 2.9 Implementation of analytical identification techniques.

sensing or direct measurement and thereafter processed by use of an identification technique. Following a survey of the existing literature, most generally identified parameters are the mutual inductance, M, and the load resistance, R_L, of the IWPT system. Although, some proposed works identify other unknown parameters such as coupling coefficient k [21], output voltage V_o [22] and output current I_o [23], with assumptions of given system parameter values such as M. Table 2.1 summarizes the status of system parameters as known (◯) , unknown (△) and sometimes known (□). Various methods in literature are classified as shown in Fig. 2.8 and discussed regarding the estimation of parameters from the primary-side of the IWPT system.

2.2.1 Analytical Techniques

Analytical methods rely on combination of mathematical models and circuit analysis equations that describe the to-be identified parameters in relation to the primary-side measured quantities. Values obtained, such as voltage or current are analyzed and utilized

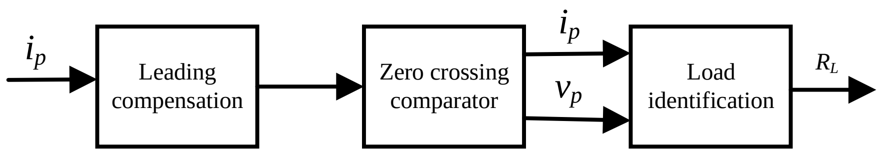

Fig. 2.10 Flowchart summary of analytical technique [24].

to estimate the targeted parameters in the system as shown in Fig. 2.9. Whether primary-side current only, primary-side voltage only, or a combination of primary-side current and primary-side voltage, these methods require different measurement information.

(a) Primary-side current measurement

A strategy for load identification is proposed to stabilize coupling-independent output power over reasonable variations in the system by only sensing the inverter output current [24]. Fig. 2.10 illustrates the followed process as the primary-side current is captured by a sensor, passed through a leading compensator to compensate for sensing delay, then converted to a voltage signal whose zero crossing is detected by a comparator. Their root mean square (rms) values are now utilized to estimate the load resistance.

With regards to battery charging applications, estimated parameters presented in [25] can be used to achieve constant-current and constant-voltage (CC-CV) charging of the lithium ion (Li-ion) battery without the need for a DC-DC converter on the receiver side. State of charge (SOC) is then calculated by use of the estimated charging current as well as the charging power is observed as the product of the estimated charging voltage and current. Equivalent resistance R_e of the secondary-side and mutual inductance M are the unknown parameters to be identified by derivations from fundamental analysis of the system demonstrated by the schematic in Fig. 2.11 and obtained as shown

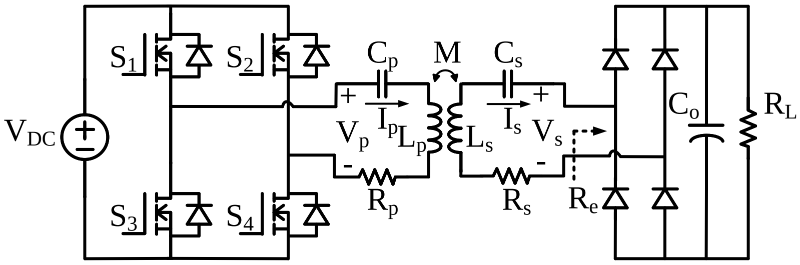

Fig. 2.11 Schematic used for load and mutual inductance identification [25].

$$R_e = \frac{(R_{in} - R_p)\left(1 - \frac{\omega_{os}^2}{\omega^2}\right)\omega L_s}{\left(1 - \frac{\omega_{op}^2}{\omega^2}\right)\omega L_p - X_{in}} - R_s \tag{2.8}$$

$$M = \sqrt{\frac{(R_{in} - R_p)\left[(R_s + R_e)^2 + \left(1 - \frac{\omega_{os}^2}{\omega^2}\right)^2 \omega^2 L_s^2\right]}{\omega^2 (R_s - R_e)}}. \tag{2.9}$$

Also, a parameter joint identification of battery charging voltage, charging current, equivalent resistance and equivalent load impedance method in [26] analyzes linear superposition of the fundamental wave together with the harmonic model of the system to realize precise estimations. Here, the input dc current is measured and the phase shift angle from the controller are utilized for parameter identification. Through analyzing the sensed primary-side current and extracting its magnitude together with its phase angle, parameter identification of the equivalent load resistance and the mutual inductance for alignment condition is presented in [27]. Extraction of the aforementioned values is performed then the estimated parameters are successively used to estimate the unknown output voltage of the secondary-side. Simple implementation is regarded as a merit in this method. However, mapping and errors from detected current signal could propagate to the estimated parameter solutions.

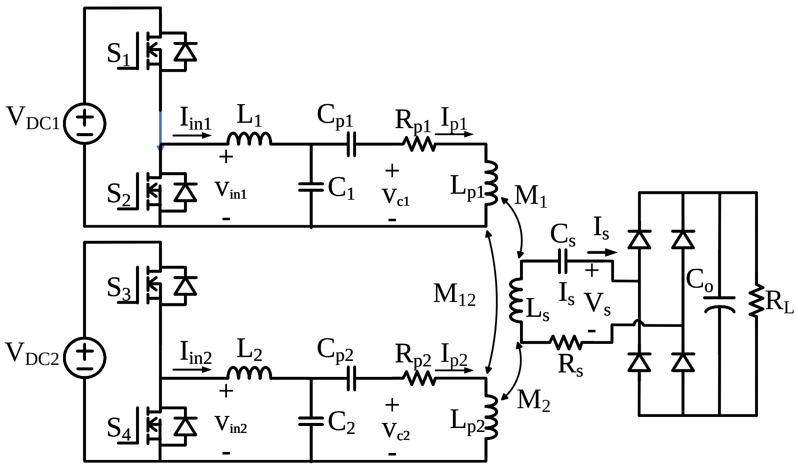

Fig. 2.12 Schematic with two transmitter coils [28].

(b) Primary-side voltage measurement

On the other hand without the need for current sensors but primary-side voltage measurement only, [28] presents a method for a system with two transmitter coils and one receiver coil. Fig. 2.12 shows the representation of this system where the secondary-side is subsequently coupled with the primary-side couplers as it changes position dynamically. It involves modeling and analysis using harmonics to steer clear of complications brought about by parameter dependency that identifies the estimation of mutual inductance between primary-side coil and secondary-side coil by solving for M_1 as shown

$$[\frac{1}{\omega C_{p1}} - \omega L_{p1}]I_{p1.n} + R_{p1}I_{p1.n} + \omega M_1 I_{s.n} - \omega M_{12} I_{p2.n} - Vc1.n = 0 \tag{2.10}$$

where M_{12}, V_{c1} and $(._n)$ are the known mutual inductance between two primary-side couplers, voltage across compensation capacitance and nth harmonic, respectively. Here as well, errors in measurement equipment could be translated to the identified parameters.

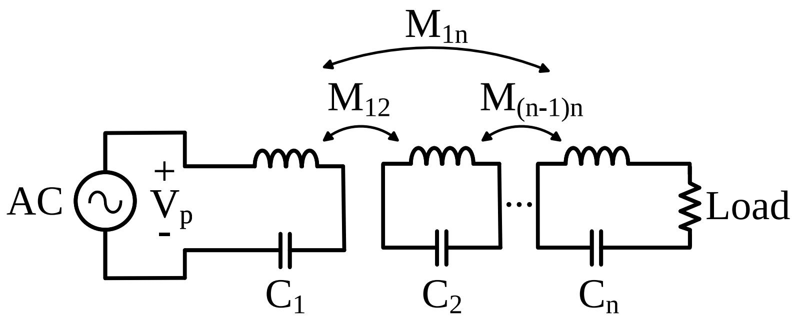

Fig. 2.13 Schematic of multiple coils system [29].

(c) Primary-side impedance measurement

Here, both the current and voltage are measured and utilized for identification. A mathematical analysis procedure involving Cramer's rule in the system matrix in [29] is employed to evaluate the sampled real time primary-side input current and voltage to derive the system's load information such as output voltage and output current of a multiple coil IWPT system. The schematic in Fig. 2.13 depicts the multiple coil IWPT system with repeater coil and secondary-side load connected to the nth coupler. The load parameters, output voltage V_o and receiver coil current I_2, are then obtained as

$$V_o = \frac{(\omega M_{12})^2 I_1 + Z_1 Z_2 I_1 - Z_2 V_p}{j\omega M_{12}} \tag{2.11}$$

$$I_2 = \frac{V_p - Z_1 I_1}{j\omega M_{12}} \tag{2.12}$$

where the subscripts represents the receiver coil number and the mutual inductance values are known. Similarly, a technique involving primary-side equivalent capacitance that is adjusted and accommodates for secondary-side receivers that have unknown or drifting resonant frequencies is proposed in [30] and analyzed to attain optimization of the system. This method requires the input current and voltage collected at fixed frequencies so as to perform

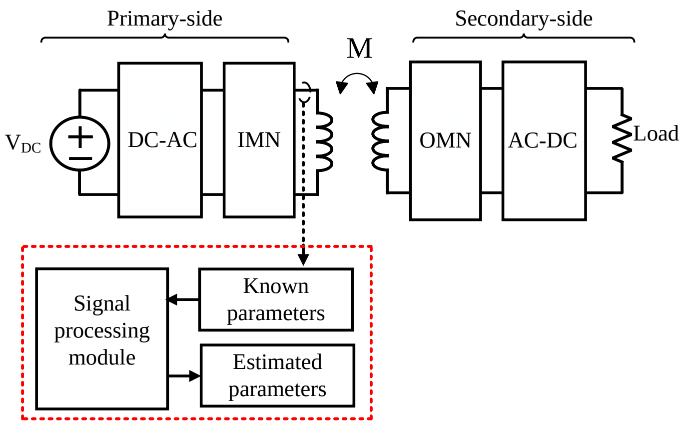

Fig. 2.14 Implementation of signal processing techniques.

the parameter identification of mutual inductance and actual resonant frequency as well as the equivalent load resistance. An advantage associated with these analytical technique is that not only is the implementation straightforward as mentioned prior, but also they provide insights into the behavior of the IWPT systems. However, the measurement errors incurred during sensing of current and voltage signals could be amplified in the process, hence large deviations in the estimated values could be seen.

2.2.2 Signal Processing-based Techniques

Signal processing-based techniques provide a valuable alternative in parameter estimation such as eliminating the need for additional hardware as they can be implemented together with the system controller and resort to various signal analysis techniques to extract information from the signals or waveforms observed on the primary-side. Fig. 2.14 demonstrates a general implementation of these techniques as the known system quantities are fed to a signal processing module which is then tasked with identifying the unknown system values. These techniques come with the advantage of suitability in dynamic operation conditions

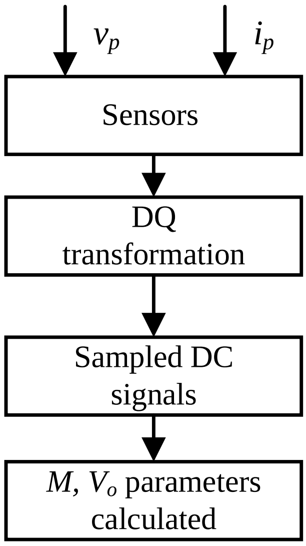

Fig. 2.15 Flowchart of the DQ identification approach [31].

besides noisy data handling capability. Here, the methods are grouped into quadrature transformation-based and Fourier transformation-based.

(a) Quadrature-based methods

In [31], a direct-quadrature (DQ) transformation technique is utilized to accurately extract the fundamental and third-order harmonic information from the sampled primary-side voltage and current waveforms. This is carried out with no restriction on the operating frequency by transforming the high-frequency signals of input voltage and current into DC signals, after passing through a DQ transformation module, for identification as illustrated by the flowchart in Fig. 2.15. Comparably, load identification approach, based on quadrature transformation (QT) [32], [33] is brought forward. As portrayed in Fig. 2.16, known values are collected, the active power P_{act} is then calculated and in turn estimation of the equivalent load resistance R_L of the battery is acquired as shown

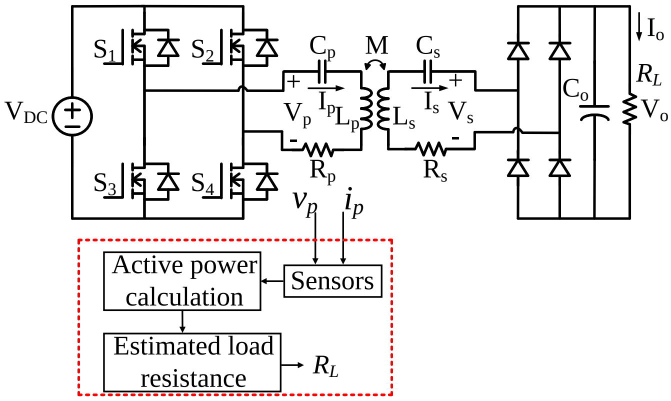

Fig. 2.16 Structure diagram of QT identification method [32].

$$P_{act} = I_{p1}^2 \left[R_p + \frac{(\omega M)^2 (R_s + R_e)(\omega C_s)^2}{(\omega C_s)^2 (R_s + R_e)^2 + (1 - \omega^2 L_s C_s)^2} \right] \tag{2.13}$$

$$R_L = \frac{\pi^2}{8} \left(\frac{(\omega M)^2 I_{p1}^2}{P_{act} - R_p I_{p1}^2} - R_s \right) \tag{2.14}$$

where I_{p1} is the rms value of fundamental component of primary-side current. This information is entered into the proposed controller to realize CC and CV charging modes by adjusting the charging current I_o and voltage V_o of the system. Detailed frequency information is availed through execution using the quadrature methods but requires high sampling rates as well.

(b) Fourier transform-based methods

Another approach is discussed in [34] where pulse density modulation is applied to generate inter-harmonics in the system. Signal acquisition of the input voltage and current via sensors is carried out prior. This is followed by a Fast Fourier Transform (FFT) that identifies the inter-harmonics via equations that are approximated using least square methods. From these equations, mutual inductance and equivalent load resistance are estimated. In [35], system operating frequency as well as inverter output voltage and current are utilized to estimate the load resistance and mutual inductance. Zero phase angle (ZPA) frequency is

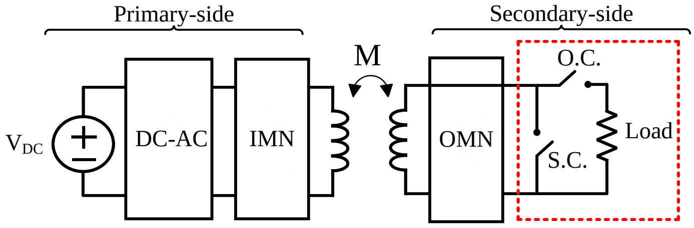

Fig. 2.17 Illustration of extreme termination state.

examined and adjusted if the system operates in another frequency as there will be a phase difference between the voltage and current. These category of techniques are suitable for variable operating conditions and noise tolerance. However, similar to the DQ methods, they may require high sampling rates in addition to intensive computations.

2.2.3 Frequency Sweeping Techniques

Mainly referring to attaining estimates of parameter values from multiple frequency sweeps, monitoring the shifts allows for observation of corresponding changes in these parameters. The discussed techniques in this section are carried out in either the extreme termination state or a load-attached state.

(a) Extreme termination sweeping

Fig. 2.17 illustrates extreme termination ways in the IWPT system. This approach is done by short-circuiting (SC) or open-circuiting (OC) the secondary-side load from the system. The study in [36] with the aid from Fig. 2.18, the SC and OC actions of the rectifier are illustrated to propose a monitoring method to estimate the coupling coefficient, k, and receiver resonant frequency, f_{os} of the system as

$$k = \sqrt{\frac{\left(f_B^2 - f_{op}^2\right)\left(f_{op}^2 - f_A^2\right)}{\left(f_A^2 + f_B^2\right) f_{op}^2 - f_A^2 f_B^2}} \tag{2.15}$$

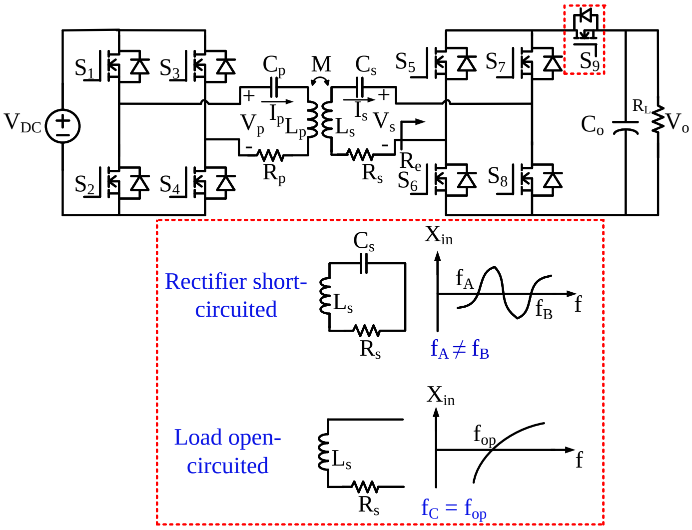

Fig. 2.18 Schematic used with extreme termination [36].

$$f_{os} = \frac{f_A f_B f_{op}}{\sqrt{\left(f_A^2 + f_B^2\right) f_{op}^2 - f_A^2 f_B^2}} \tag{2.16}$$

where f_A, f_B are two ZPA frequencies and f_{op} is the resonant frequency of the primary-side. Key aspect of this technique is determining the ZPA frequencies of the system when the imaginary part of the primary-side input impedance is zero through frequency sweeping process known as frequency shift keying (FSK) modulation with the secondary-side rectifier kept momentarily either short-circuited or open-circuited. This requires one additional phase detection sensor for the primary-side current to carry out the estimation. Another way is proposed in [21] where the authors have analyzed and evaluated several adaptive frequency step functions that are intended for the coupling coefficient k identification. After a short-circuit action of the active rectifier in the secondary-side, a sweep of the switching frequency is carried out to achieve a critical frequency point $f(n)$ when $X_{in} = 0$ by comparing the power factor (PF) value to a set reference. The process is as illustrated in Fig. 2.19, and

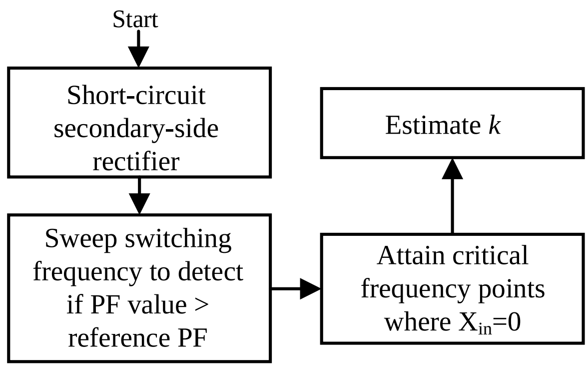

Fig. 2.19 Identification following extreme termination [21].

considering f_o as the resonant frequency k_n calculated at the critical frequency point is

$$k_n = \frac{f_o^2}{f^2(n)} - 1. \tag{2.17}$$

Mutual coupling coefficient determined through the use of active rectifiers is proposed in [37]. In this work, current information from the current sensor and the output voltage from the power inverter are utilized to measure the phase difference after momentarily short-circuiting the rectifier outputs. Hence estimation process is then undertaken. Implemented in a digital controller, inverter's frequency scanning is performed within set sweeping boundaries to deduce the frequency operating points when pulse width transmitter voltage and current is zero. Although it is an intrusive method to the system operation for frequency sweeps, real-time identification is needed for estimating the target parameters.

(b) Load-attached sweeping

As summarized in the flowchart of Fig. 2.20, identification is carried out while load is kept intact which does not halt the system operation unlike the extreme termination approach carried out prior. For front-end monitoring of multiple loads presented in [38], an n-coil

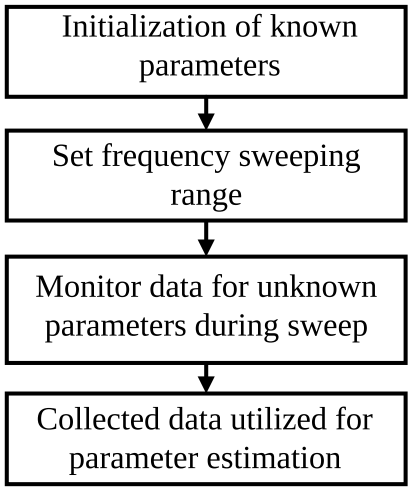

Fig. 2.20 Flowchart of identification in load-attached state.

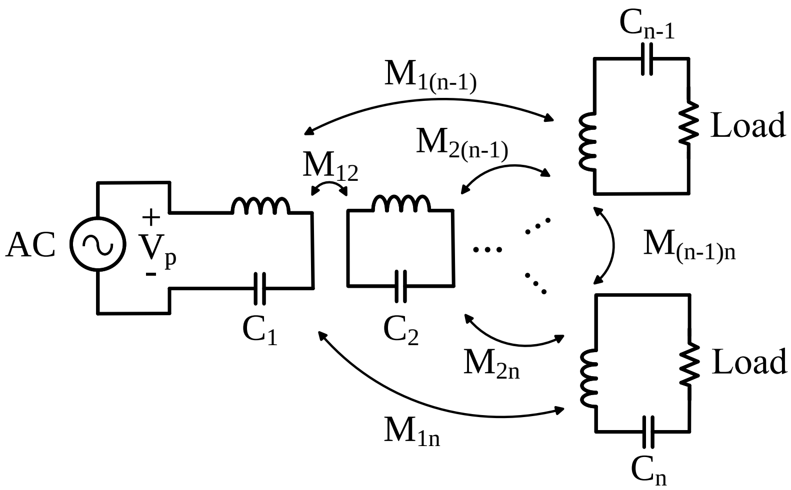

Fig. 2.21 Schematic of n-coil IWPT system with two attached loads [38].

IWPT system is presented. Fig. 2.21 shows a schematic of an n-coil IWPT system with a relay coil and two secondary-side loads. Accurate estimates of the value of the loads are obtained from multiple frequency sweeping scans with load connected to the system and also least square method is used to overcome effects of noise and tolerance, which makes it effective in real-time identification. In a like manner to simultaneously estimate load resistance, mutual inductance, and receiver coil inductance [39], frequency sweep combined with a gradient descent method is presented. Additional merit to this technique is that the inductance identification technique can also serve as a way to detect foreign metal objects when the mutual inductance estimation results deviate far from the nominal inductance. Through measuring the input voltage, current, and phase angle at the operating frequency, the mutual inductance M and load resistance R_L are identified in [40] through the equations below.

$$M = \sqrt{\frac{\omega L_s - \frac{1}{\omega C_s}}{\omega^2 Im\left[Z_{in}(j\omega) - Z_a(j\omega)^{-1}\right]}} \tag{2.18}$$

$$R_L = \frac{\omega L_s - \frac{1}{\omega C_s}}{\left[Z_{in}(j\omega) - Z_a(j\omega)\right] Im\left[Z_{in}(j\omega) - Z_a(j\omega)^{-1}\right]} - Z_b(j\omega) \tag{2.19}$$

where $Im(.)$ is the imaginary part operator, and $Z_a(j\omega)$ and $Z_b(j\omega)$ are defined as

$$Z_a(j\omega) = j\omega L_p + \frac{1}{j\omega C_p} + R_p \tag{2.20}$$

$$Z_b(j\omega) = j\omega L_s + \frac{1}{j\omega C_s} + R_s + R_e. \tag{2.21}$$

This method requires the sweeping frequency to be around the resonant frequency of the secondary-side for estimation accuracy purpose. As this method dynamically monitors the coupling conditions of the primary and secondary couplers, their positions can change a bit freely. An identification method for bidirectional IWPT system is proposed in [41] where superposition principle is applied for current decoupling, which is described as dividing the primary-side current into a primary-side voltage-dependent part and a secondary-side voltage-dependent part, and identification of the mutual inductance is achieved by adjusting the primary-side converter's frequency until the reactive power is equivalent to zero. The use of current decoupling allows the estimation of mutual inductance at start-up and secondary-

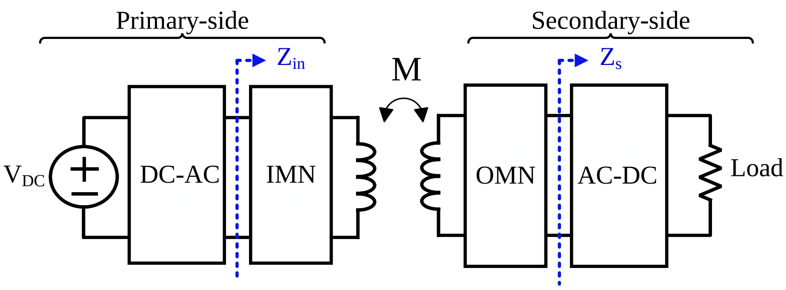

Fig. 2.22 Representation of IWPT system impedances.

side phasor information is scanned continuously making the technique adaptable to varying operation conditions. However, in case of slight variation this method might be more sensitive to disturbance during estimation and requires continued monitoring of the system for frequency information.

2.2.4 Impedance Characteristic-based Techniques

In these techniques, general system impedance as illustrated in Fig. 2.22 are made use of to infer parameter estimations. As variations in receiver circuit affect the impedance into the rectifier Z_s and/or the impedance Z_{in} seen from the inverter, these changes are then taken into consideration in the identification. Impedance variation analysis and primary-side voltage-current phase angle analysis are two ways found in the proposed techniques that utilize impedance characteristics.

(a) Impedance variation analysis

Dual impedance identification method is proposed to estimate output parameters R_e and L_e through an iterative process using least mean squares (LMS) adaptive filter algorithm to compute load resistance R_L [42]. The schematic in Fig. 2.23 shows the equivalent circuit of the aforementioned system where the Z_{in} is the input impedance seen from the primary-side

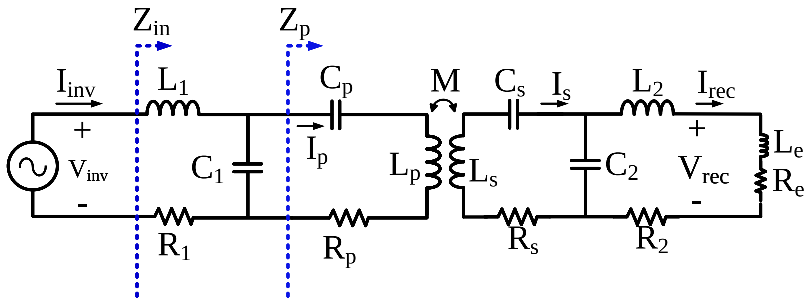

Fig. 2.23 Equivalent circuit of the dual impedance identification approach [42].

inverter while Z_p is the primary-side compensation impedance. The attained equivalent resistance R_e as well as equivalent inductance L_e are as shown

$$R_L(n+1) = R_L(n) + 2e(n)|Z_{p\_meas}||Z_{in\_meas}| \tag{2.22}$$

$$R_e = \frac{8\omega^2 L_2^2 R_L}{(\pi - 8/\pi)^2 R_L^2 + \pi^2\omega^2 L_2^2} \tag{2.23}$$

$$L_e = \frac{8(\pi - 8/\pi)^2 L_2 R_L^2}{(\pi - 8/\pi)^2 R_L^2 + \pi^2\omega^2 L_2^2} \tag{2.24}$$

where n refers to the number of iterations and e is the step size of the iterations. In this work, the equivalent series inductance L_e of the load is also considered to improve the accuracy of the load identification. Equivalent impedance modulus expressions of Z_{in} and Z_p are obtained from measurements following which substitutions iteratively solves for parameter estimation. A study in [43] establishes a system that works under two different sets of parameters because of the changing of compensation capacitance in the primary-side circuit. Combined with the reflected impedance equation together with system operating parameters such as the measured input DC voltage, rms of the detected input current and primary-side resonant frequency, ultimately achieve the mutual inductance and load identification as depicted by

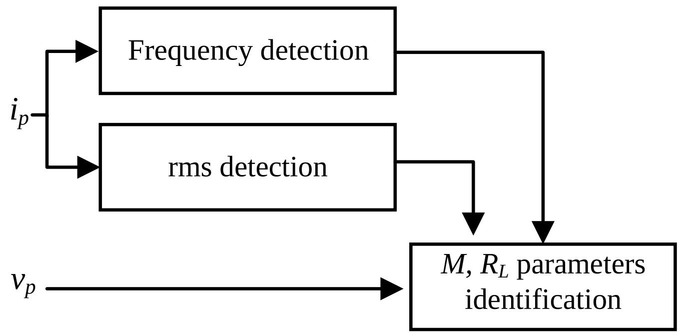

Fig. 2.24 Impedance variation-based identification diagram [43].

the diagram in Fig. 2.24. As seen, this method offers direct measurement to obtain values of known system parameters to valuate system impedances.

(b) Impedance phase angle analysis

Similarly offering a direct measuring approach, [44] proposes a primary-side linear control strategy to realize constant CC and CV charging for IWPT system, utilizing input impedance characteristics of the rectifier for improved accuracy of system parameter estimation. Primary-side voltage and current are sensed, and a linear relationship among input voltage, load current and load voltage is established. In the case of multiple transmitter coils discussed in [45], the demonstration in Fig. 2.25 shows a schematic of n primary-side couplers and one secondary-side coupler of the proposed dynamic wireless power transfer system. Phase difference between current and voltage of each transmitting coil and the receiving coil as well as the active and inactive coils is measured, providing an intuitive look into the system resonances as analysis of the net reflected impedance Z_{f1} to the primary-side from the secondary-side impedance Z_s is carried out. This is then employed to identify the mutual inductance M_1 with respect to first transmitter as shown

$$Z_{f1} = \frac{\omega^2 M_1^2}{Z_s} \tag{2.25}$$

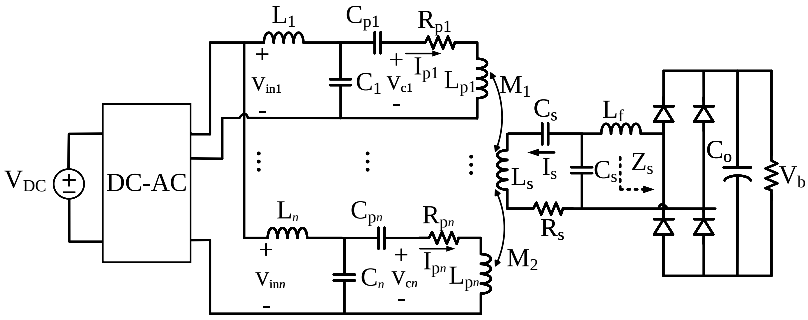

Fig. 2.25 Schematic of a multiple coil dynamic IWPT system [45].

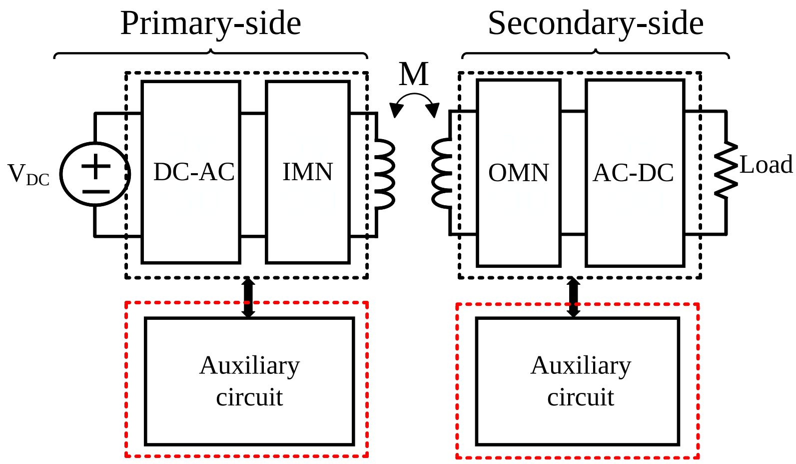

Fig. 2.26 Auxiliary circuit implementation in IWPT system.

$$M_1 = \frac{|Z_s|}{\omega}\sqrt{\frac{R_{f1}}{Re(Z_s)}} \tag{2.26}$$

where R_{f1} is the real part of Z_{f1} and $Re(Z_s)$ is the real part of equivalent impedance of the secondary-side. This too is shown to be advantageous in giving insight into impedance information reflected to the transmitting side. However, the complexity exists here as it may require a wide frequency range to perform the intended analyses.

2.2.5 Auxiliary Circuit-based Techniques

With the aim to improve responsiveness, auxiliary components such as extra coils or even whole circuitry are implemented exclusively for identification purposes. This technique

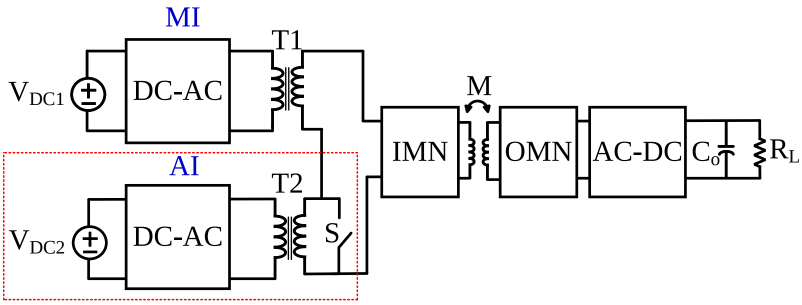

Fig. 2.27 Auxiliary inverter concept [46].

possesses an advantage where difficult-to-measure values such as coupling coefficient can be obtained and system uninterruption during identification process. Fig. 2.26 illustrates a general circuit implementation of auxiliary circuit-based techniques which are realized either on the primary-side, secondary-side, or both sides of the IWPT system.

(a) Primary-side implementation

Based on an auxiliary inverter (AI) and a main inverter (MI) in [46], an identification method for mutual inductance and load parameter has been presented. The MI and AI are designed to operate in resonant and non-resonant modes, respectively, along with two series-connected transformers, $T1$ and $T2$, as depicted in Fig. 2.27. The switch S has the role of disconnecting the AI during resonant mode when turned on and connecting AI to the system during non-resonant mode as the operating frequencies of MI and AI are inconsistent. The magnitude of primary-side current waveform is acquired and utilized to attain the estimated parameter values of the mutual inductance and equivalent load resistance. Correspondingly with no action needed from the secondary-side, phase information of the secondary-side current is detected by implementation of zero crossing sensor with another sensing coil pick-up that contains a large resistance $R_{sensing}$ which is decoupled from the primary-side [47]. This is illustrated by the schematic in Fig. 2.28 where the auxiliary

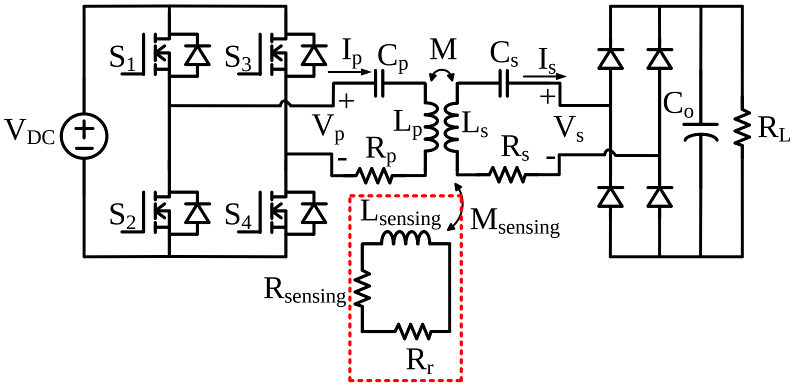

Fig. 2.28 Schematic of auxiliary sensing circuit [47].

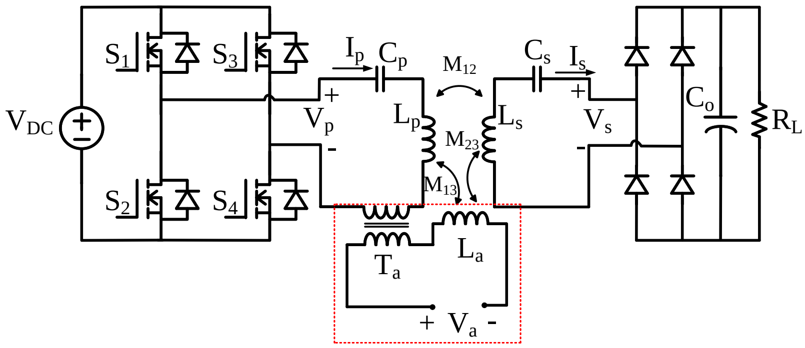

Fig. 2.29 Auxiliary coil and transformer implementation [48].

sensing circuit is coupled with the secondary-side winding via mutual inductance $M_{sensing}$ but decoupled from primary-side winding, with $L_{sensing}$ and R_r as the inductance and ESR of the sensing circuit, respectively. Estimation of the coupling coefficient together with the secondary-side resonant frequency is then performed with only primary-side resonant frequency and secondary-side resonant frequency is not required to be known prior. In the work of [48], a primary-side-integrated auxiliary circuit as seen in Fig. 2.29 with a coupler L_a and a primary-side isolated transformer T_a to improve the accuracy in charging voltage and current estimation is proposed to achieve high precision within a reasonable horizontal misalignment range. Equations derived to estimate the parameters are attained using the measured voltage across auxiliary pick-up coil which is denoted as V_a as shown in

$$I_o = \frac{2\sqrt{2}}{\pi\omega M_{23}} V_a = \frac{8}{\pi^2(\omega M_{12})} V_{DC} cos\left(\frac{\alpha}{2}\right) \tag{2.27}$$

$$V_o = \frac{\omega^2 M_{12} C_p}{\omega^2 L_p C_p - 1} V_{DC} cos\left(\frac{\alpha}{2}\right) \tag{2.28}$$

where α, M_{12} and M_{23} are phase-shift angle, known mutual inductance values between primary-side and secondary-side, and secondary-side and auxiliary coil, respectively. With the auxiliary circuit having the main role of parameter identification, the system operation is uninterrupted during the estimation process contributing to less identification errors. On the other hand, extra circuitry implies system complexity in hardware implementation.

(b) Secondary-side implementation

In [49], as shown in Fig. 2.30, an auxiliary calibration circuit consisting of a switch S_{cal}, a voltage clipper for protection, a resistor R_{cal} and a frequency detector to facilitate mutual inductance identification is presented. Here, two processes take place sequentially where mutual inductance M is determined in the first calibration process with the calibration switch off, which is controlled by information from the frequency detector, then the second charging process follows to charge the battery in CC and CV modes. The estimated mutual inductance M as well as the charging current I_b and voltage V_b are therefore calculated as

$$M = \frac{4\left(V_{oH} + 2V_D\right)}{\pi\omega I_{p1sat}} \tag{2.29}$$

$$I_b = \frac{2}{\pi\omega M} V_{p1} \tag{2.30}$$

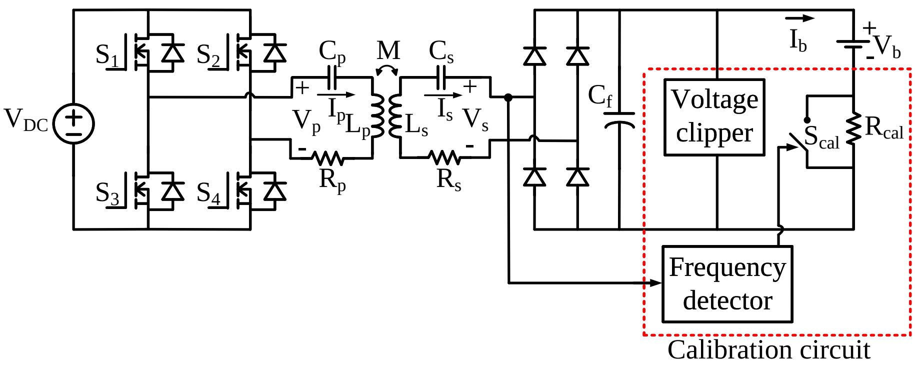

Fig. 2.30 Secondary-side auxiliary calibration circuit [49].

$$V_b = \frac{\pi\omega M}{4} I_{p1} - 2V_D \tag{2.31}$$

where V_{oH}, V_D, I_{p1sat}, I_{p1} and V_{p1} are the specified upper output voltage limit, diode forward voltages, saturated current of the transmitter side, amplitude of primary-side current and amplitude of primary-side voltage, respectively. V_{oH} limits the battery charging voltage V_b when I_{p1sat} reaches a set value, and identification is completed as shown above. Seeing as this secondary-side implementation method mirrors that of primary-side implementation, it is considered that main disadvantage is added components to one side of the system to perform the same role of identification.

(c) Dual-side implementation

A dual-side phase-shift implementation is proposed using driving windings on both primary-side and secondary-side of the system as illustrated in Fig. 2.31 [50]. The subscripts (P) and (D) represent the main power winding and driving winding in this IWPT system, respectively. These driving windings are quadruple-D coils with a minimized turn number such that only small power is present, and are decoupled from the main power windings. Current in the primary-side driving winding induces a voltage in the secondary-side driving

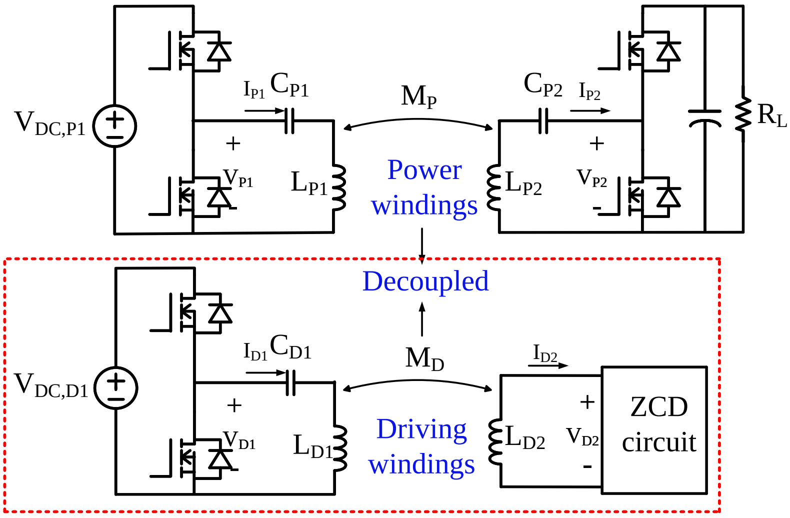

Fig. 2.31 Dual-side auxiliary circuits implementation [50].

winding, which act as the zero current detection (ZCD) circuit that detect the zero crossing of the secondary-side voltage to generate a delayed signal respective to voltage in secondary-side main winding. Secondary-side current and output power are therefore identified. The advantage offered by this method is isolation of the auxiliary circuits from the main power circuit. However, the accompanying downside is that the required additional hardware then introduces more losses to the overall system.

2.2.6 Comparative Summary

A comparative summary of the discussed front-end system parameters identification techniques is illustrated in Table 2.2. In conclusion, primary-side system parameter identification techniques play a major role when it comes to eliminating any type of communication between primary-side and secondary-side of the IWPT system. It is essential to determine the parameter values through estimation so as to understand the system characteristics such as mutual coupling. Table 2.3 provides a summary of comparative analysis of primary-side identification techniques proposed in literature and Fig. 2.32 presents a visualization of the

Table 2.2 Summary of primary-side identification techniques.

Identification technique	Principle	Advantages	Disadvantages	Ref.
Analytical techniques	Mainly utilize mathematical model or circuit analysis	Relatively simple implementation, provides insight into system behaviors	Errors easily translated to solutions, accurate model assumptions required, sensitive to measurement inaccuracy	[24],[25], [26], [27], [28], [30]
Signal processing-based techniques	Uses signal processing methodologies to extract and examine parameters	Dynamic condition suitability, noisy signal handling capability, detailed frequency information attainable	Computationally intensive, higher sampling rates might be required, advanced algorithms required	[31], [32], [34], [35]
Frequency tracking-based techniques	Performs frequency sweeps to track changes and identify parameters	Adaptable to varying operating conditions, effective in real-time identification, non-intrusive to system operation	Continuous monitoring required, sensitivity to noise and disturbance, complex implementation	[36], [21], [37], [38], [39], [40]
Impedance characteristic-based techniques	Measure and analyze variations in impedances of the system	Direct measurement approach, insight into system impedance information, non-intrusive to system operation	Complex impedance calculations, sensitivity to variations, might require a wide frequency range	[42], [43], [44], [45]
Auxiliary circuit-based techniques	Implements auxiliary components that are used for identification	High identification accuracy, applicable for difficult-to-measure parameters, can be isolated from the main system	Additional hardware required, increased system complexity, might introduce additional losses to the system	[46], [47], [48], [49], [50]

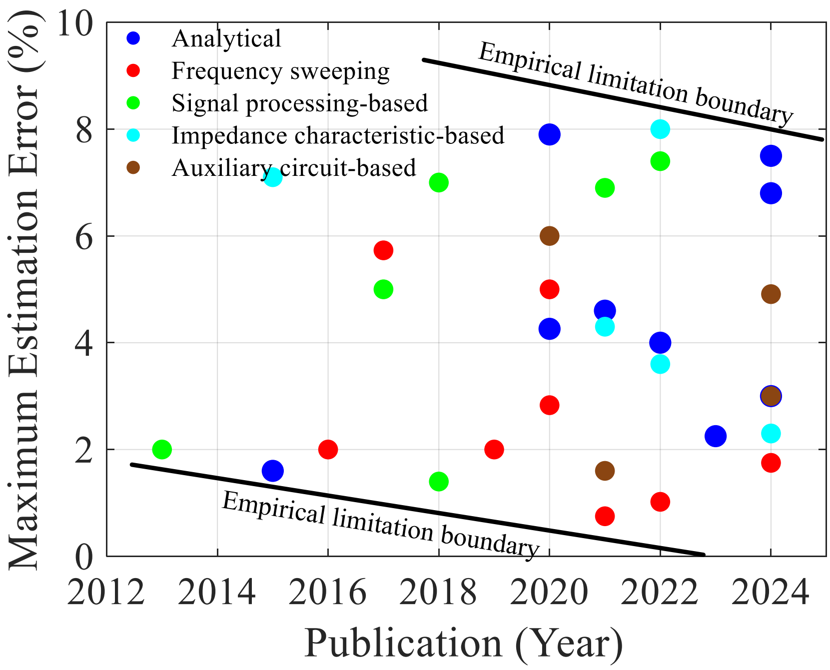

Fig. 2.32 Maximum estimation error data from literature.

Table 2.3 Comparative analysis of primary-side identification techniques.

Ref.	Static/Dynamic application	Online (On)/Offline (Off) identification	Estimated parameters	Maximum estimation time (ms)	Maximum estimation error (%)
[10]	Static	On	M	-	4
[31]	Dynamic	On	M, V_o, P_o	7.0	6.9
[25]	Dynamic	On	M, R_L	10.0	6.8
[23]	Dynamic	Off	V_o, I_o, R_L	-	2.6
[28]	Dynamic	-	M, R_L	-	3
[36]	Static	On	k, f_s	2.5-8	1.75
[32]	Static	-	R_L	-	1.4
[51]	Static	On	M, V_o, I_o	-	6.64
[48]	Dynamic	-	-	-	1.6
[40]	Dynamic	-	M, R_L	-	<2
[35]	Static	-	M, R_L	-	<7
[24]	Static	On	R_L	-	4.26
[22]	Static	On	V_o	-	2.83
[21]	Static	-	k	<7	<1.02
[29]	Static	-	R_L	-	1.6
[52]	Dynamic	On	M, I_o	-	5.6
[53]	Dynamic, Static	On	M, R_L	5.6	3.1
[37]	Static	-	k	62	<5
[26]	Dynamic	-	R_L, Z_L, V_o, I_o	-	<7.9
[46]	Dynamic	On	M, R_L	-	<6
[41]	Static	-	M	-	0.75
[43]	Dynamic	On	R_L	50	7.1
[54]	Static	Off	M, R_L	-	-
[49]	Static	-	M	20	<3
[47]	Static	Off	k, f_s	5-9	4.91
[55]	Dynamic	Off	M	-	6.53
[25]	Dynamic	On	M, R_L	-	6.8
[56]	Static	-	V_o, R_L	-	4.3
[45]	Dynamic	Off	M, R_L	-	8
[27]	Static	On	M, R_L, V_o	20	5
[57]	Dynamic	-	M, R_L	-	4.6
[58]	Static	On	k, Q_p, Q_s	-	5.73
[59]	Static	On	R_L	-	2
[30]	Dynamic	-	M, R_L, f_r	-	7.5
[60]	Dynamic	On	R_L	85	2.25
[34]	Static	On	M, R_L	-	7.4
[61]	Dynamic	On	k, R_L	3.8	2.1
[62]	Dynamic	On	M	-	<4
[44]	Static	-	V_o, I_o, R_L	-	3.6
[39]	Dynamic	-	M, R_L, L_s	-	2
[63]	Static	-	R_L, L_s	-	-
[42]	Static	On	M, R_L	8-17	2.33

Note: Q_p = Primary-side quality factor, Q_s = Secondary-side quality factor, (-) = Unspecified.

maximum estimation errors against publication time in years. It can be seen that in the recent years the maximum estimation error range is clustered approximately between 1 % and 5 %. The frequency sweeping techniques tend to approach the lower limitation boundary due to their merit of noise handling capability while proneness to error of analytical techniques and impedance characteristic-based technique dominate the average almost reaching the upper empirical boundary due to propagation errors in their calculations. Auxiliary circuit-based techniques as well as signal processing-based techniques involve complexities in their implementations which reflects to their average trend on the error estimation results plot. Furthermore, the gathered data reveals a general downward trend of the estimation error over time, indicating progressive improvement of the proposed techniques.

2.3 Conclusion of the Chapter

This chapter has presented an extensive literature survey into system parameter identification for primary-side control in IWPT systems. In literature, a huge body of work has proposed numerous techniques on how to obtain system parameter values and achieve system optimization in both static and dynamic power transfer applications. Focus has been placed on exploring and conducting an investigation on the aspect of research in IWPT system technology without any wireless communication between the secondary-side and the primary-side. Various proposed front-end system estimation techniques have been classified into analytical-based, signal processing-based, frequency tracking-based, impedance characteristic-based and auxiliary circuit-based methods.

Chapter 3

Conventional Analytical Identification

As has been discussed extensively in Chapter 2, various topologies have been applied in the IWPT system operations. For the parameter identification analysis in this chapter, the SS-compensated IWPT system is utilized as illustrated in Fig. 3.1. Through this, the limitations associated with conventional sole analytical identification are investigated to establish the motivation for the proposed identification approach.

3.1 Limitations Associated with Conventional Sole Analytical Approaches of Parameter Identification

Sole analytical-based conventional identification is based off of the system equivalent circuit model. The equivalent circuit schematic of the SS-compensated IWPT system is shown in Fig. 3.2. Assuming fundamental harmonic approximation using the Kirchhoff's

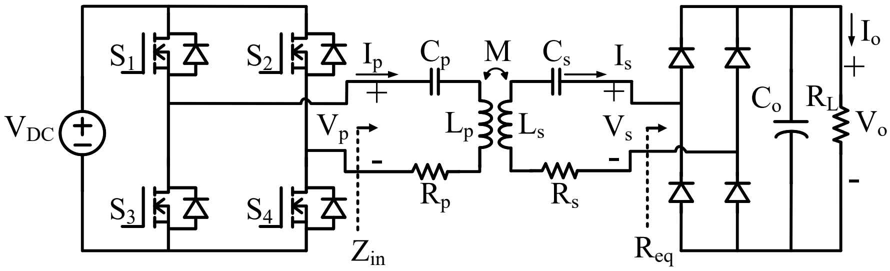

Fig. 3.1 Schematic of series-series compensated IWPT system.

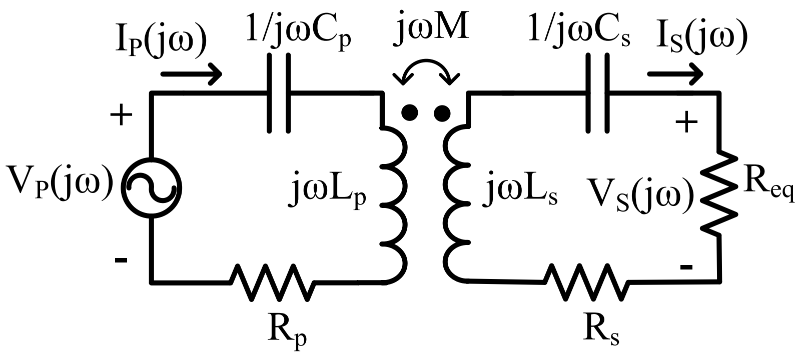

Fig. 3.2 Equivalent circuit of SS-compensated IWPT system.

voltage law (KVL) analysis, the equivalent input impedance Z_{in} seen from the primary side is obtained to be

$$Z_{in} = R_p + j\omega L_p + \frac{1}{j\omega C_p} + \frac{(\omega M)^2}{Z_s} \tag{3.1}$$

where Z_s is the secondary-side impedance given as

$$Z_s = R_s + j\omega L_s + \frac{1}{j\omega C_s} + R_{eq}. \tag{3.2}$$

From (3.1), the real part, R_{in}, and imaginary part, X_{in}, of the equivalent input impedance are separated as

$$Z_{in} = R_{in} + jX_{in} \tag{3.3}$$

where

$$R_{in} = R_p + \frac{\omega^2 M^2 (R_s + R_{eq})}{(R_s + R_{eq})^2 + (\omega L_s - 1/\omega C_s)^2} \tag{3.4}$$

and

$$X_{in} = \omega L_p - \frac{1}{\omega C_p} - \frac{(\omega L_s - 1/\omega C_s)\,\omega^2 M^2}{(R_s + R_{eq})^2 + (\omega L_s - 1/\omega C_s)^2}. \tag{3.5}$$

(3.4) and (3.5) are simplified by equating same denominator terms on the right-hand side to obtain

$$\frac{\omega^2 M^2 (R_{eq} + R_s)}{R_{in} - R_p} = \frac{(\omega L_s - 1/\omega C_s)}{X_{in} - \omega L_p + 1/\omega C_p} \tag{3.6}$$

and thus, estimated equivalent AC load resistance can be derived as

$$R_{eq} = -\frac{(R_{in} - R_p)(\omega L_s - 1/\omega C_s)}{X_{in} - \omega L_p + 1/\omega C_p} - R_s. \tag{3.7}$$

This R_{eq} is transformed to the estimated load resistance R_L by the power balance of the lossless full bridge rectifier as

$$R_L = \frac{\pi^2}{8}\left(-\frac{(R_{in}-R_p)(\omega L_s - 1/\omega C_s)}{X_{in}-\omega L_p + 1/\omega C_p} - R_s\right). \tag{3.8}$$

The rms of the fundamental component of the voltage across R_{eq} in 3.7 is given by

$$V_{s1,rms} = I_{s1,rms} R_{eq} \tag{3.9}$$

where $I_{s1,rms}$ is the rms of the fundamental component of the secondary-side current given by

$$I_{s1,rms} = \left|\frac{j\omega M I_{p1,rms}}{Z_s}\right|. \tag{3.10}$$

Hence, the full-wave bridge rectifier produces approximately the average value of the full-wave rectified output load voltage [25] as

$$V_o = \frac{\pi}{2\sqrt{2}}\left|\frac{j\omega M I_{p1,rms}}{R_s + j\omega L_s + 1/j\omega C_s + R_{eq}}\right| R_{eq}. \tag{3.11}$$

These estimations for load resistance (3.8) and output load voltage (3.11) are executed with the aid of measured primary-side current and voltage to determine the R_{in} and X_{in} terms as

$$R_{in} = \frac{V_{p1,rms}}{I_{p1,rms}}\cos\theta \tag{3.12}$$

and

$$X_{in} = \frac{V_{p1,rms}}{I_{p1,rms}}\sin\theta \tag{3.13}$$

where $V_{p1,rms}$ and $I_{p1,rms}$ are the rms values of the fundamental components of the primary-side voltage and current, respectively, and θ is the phase difference between fundamental components of the primary-side voltage and current during operation.

To illustrate noise impact on the sole analytical identification method, the process begins with raw, noisy sensed quantities of the primary-side voltage and current. These noisy signals, $v_{\mathrm{p,sens}}(t)$ and $i_{\mathrm{p,sens}}(t)$, can be modelled as the sum of the true signal and additive white Gaussian noise (AWGN) terms

$$v_{\mathrm{p,sens}}(t) = v(t) + n_v(t) \tag{3.14}$$

where

$$n_v(t) \sim \mathcal{N}(0, \sigma_v^2), \tag{3.15}$$

and

$$i_{\mathrm{p,sens}}(t) = i(t) + n_i(t) \tag{3.16}$$

where

$$n_i(t) \sim \mathcal{N}(0, \sigma_i^2). \tag{3.17}$$

Here, the variances σ_v^2 and σ_i^2 quantify the noise introduced by the voltage and current sensors, respectively, with zero mean. These noisy, instantaneous signals are then processed to calculate their rms values. This step carries the noise from the time domain into the estimated parameters. The resulting noisy rms values can be approximated as the true rms value plus an equivalent noise amplitude N_v

$$V_{\mathrm{p1,rms,sens}} \approx V_{\mathrm{p1,rms,true}} + N_v \tag{3.18}$$

and N_i

$$I_{\text{p1,rms,sens}} \approx I_{\text{p1,rms,true}} + N_i. \tag{3.19}$$

These noisy sensed values are the direct inputs for calculating the input impedance of the system using (3.12) and (3.13). Consequently, the calculated impedance parts, R'_{in} and X'_{in}, will also be erroneous, composed of their true values plus noise-induced error terms, δR_{in} and δX_{in} as

$$R'_{in} = \frac{V_{\text{p1,rms,sens}}}{I_{\text{p1,rms,sens}}} \cos\theta \tag{3.20}$$

$$= R_{in} + \delta R_{in} \tag{3.21}$$

and

$$X'_{in} = \frac{V_{\text{p1,rms,sens}}}{I_{\text{p1,rms,sens}}} \sin\theta \tag{3.22}$$

$$= X_{in} + \delta X_{in}. \tag{3.23}$$

The propagation of these intermediate errors influences the estimation of the equivalent load resistance, R'_{eq}, modifying the formula in (3.7). To explore how, R_{eq} is linearized around R_{in} and X_{in} using a first-order Taylor expansion to give

$$\begin{aligned} R'_{eq} &= f(R'_{in}, X'_{in}) \\ &\approx f(R_{in}, X_{in}) + \left.\frac{\partial f}{\partial R_{in}}\right|_{(R_{in},X_{in})} \delta R_{in} \\ &+ \left.\frac{\partial f}{\partial X_{in}}\right|_{(R_{in},X_{in})} \delta X_{in}. \end{aligned} \tag{3.24}$$

Hence, the estimation error can be written as

$$\delta R_{eq} = R'_{eq} - R_{eq} \tag{3.25}$$

$$\approx \frac{\partial R_{eq}}{\partial R_{in}} \delta R_{in} + \frac{\partial R_{eq}}{\partial X_{in}} \delta X_{in}. \tag{3.26}$$

Since δR_{in} and δX_{in} are assumed to be zero-mean and are uncorrelated, then the variance of δR_{eq} can be expressed as the weighted sum of the variances of δR_{in} and δX_{in}, which are given by the squared partial derivatives

$$\mathrm{Var}[R'_{eq}] \approx \left(\frac{\partial R_{eq}}{\partial R_{in}}\right)^2 \mathrm{Var}[\delta R_{in}] + \left(\frac{\partial R_{eq}}{\partial X_{in}}\right)^2 \mathrm{Var}[\delta X_{in}]. \tag{3.27}$$

Noting that the output voltage V_o in (3.11) depends on R_{eq}, any uncertainty in R_{eq} will be propagated into V_o. Denoting this dependence as

$$V_o \propto g(R_{eq}) \tag{3.28}$$

where g represents the other quantities in the equation, linearizing gives

$$V'_o \approx V_o + \frac{\partial V_o}{\partial R_{eq}} \delta R_{eq}. \tag{3.29}$$

Therefore, the variance of the estimated output voltage is

$$\mathrm{Var}[V'_o] \approx \left(\frac{\partial V_o}{\partial R_{eq}}\right)^2 \mathrm{Var}[R'_{eq}]. \tag{3.30}$$

The expression in (3.27) shows that the initial measurement variances, which originate from σ_v^2 and σ_i^2, are amplified by the square of the factors inherent in the identification formula. This explains that the sole analytical approach is structurally prone to noise as it is propagated in subsequent operations. The error in the estimated load resistance is cascaded to the final output voltage estimation. The resulting variance of the estimated output voltage, $\mathrm{Var}[V_o']$, demonstrates a dependence on the load resistance estimation variance. Hence,

$$\delta R_L = R_L' - R_L \tag{3.31}$$

and

$$\delta V_o = V_o' - V_o. \tag{3.32}$$

are the resulting error terms of the estimated parameters.

3.2 Noise impact of Sole analytical-based conventional identification

Utilizing the system specifications provided in Table 3.1 and assuming that the system operation is at/close to resonance condition, load resistance and output load voltage are estimated using analytical-based conventional identification by utilizing PSIM simulations. Fig. 3.3 (a) and (b) provides a quantitative demonstration of (3.27) and (3.30), respectively, plotting the increasing primary-side current noise variance of 0.01^2 to 0.05^2 against the variance of the estimated load resistance R_L and output voltage V_o. Also, the signal noise is considered in the current measurement since because the sinusoidal current is more sensitive to noise compared to square wave voltage. This is because current sensors, such as current

Table 3.1 Circuit parameters for simulation and experiment.

Symbol	Parameters	Value
L_p	Primary coil self-inductance	155.40 μH
L_s	Secondary coil self-inductance	156.56 μH
M	Mutual inductance	41.54 μH
C_p	Primary-side compensation capacitance	15.88 nF
C_s	Secondary-side compensation capacitance	16.30 nF
R_p	Primary coil equivalent series resistance	0.1434 Ω
R_s	Secondary coil equivalent series resistance	0.1474 Ω

transformers or Hall effect sensors, output a very low voltage signal which is can be corrupted easily. In Fig. 3.3 (a), the variance of the estimated R_L rises from less than 0.01 Ω^2 to approximately 0.24 Ω^2 while Fig. 3.3 (b) shows that the variance of V_o increases from less than 0.01 Ω^2 to approximately 0.12 V_o^2. The accelerating growth in the variance of both estimates demonstrates that the conventional sole analytical method inherently amplifies measurement uncertainty, leading to unreliable and imprecise results as noise increases.

Fig. 3.4 demonstrates the consequence of this unreliability by plotting the mean percentage error due to the variance of the resulting terms in (3.31) and (3.32) across the variance range. It can be seen that the mean percentage error of the estimated R_L in Fig. 3.4 affects the estimation of the V_o by approximately 0.58% at a noise variance of $\sigma^2 = 0.0025$. This effect is observed in the deviating estimation error at the same variance for simulation in Fig. 3.5 with R_L and V_o estimations. It is illustrated that the increased variance from (3.27) and (3.30), translates into reduced estimation accuracy for both the estimated R_L and the subsequent V_o parameters estimation.

Fig. 3.5 (a) demonstrates the R_L estimation while Fig. 3.5 (b) shows the V_o estimation with $\sigma^2 = 0.0025$ injected noise variance. From this demonstration it can be seen that the

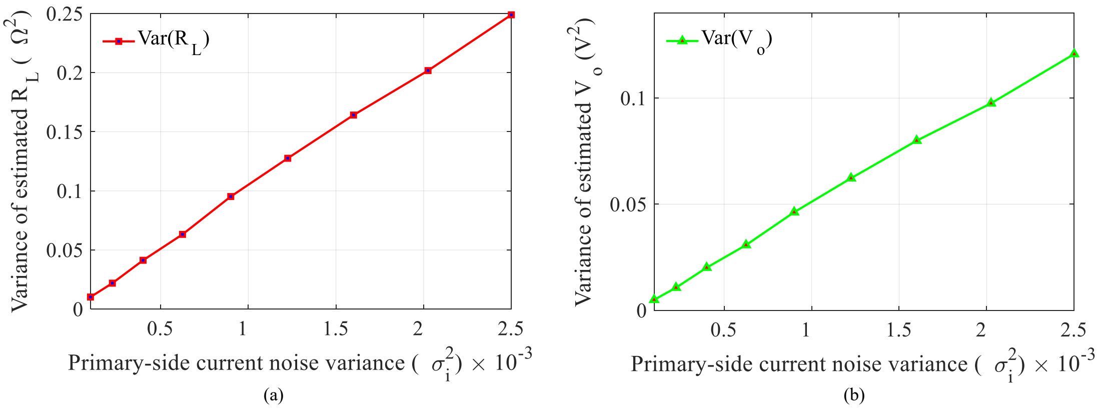

Fig. 3.3 Effect of sensed noise variance on the variance of estimated R_L and V_o.

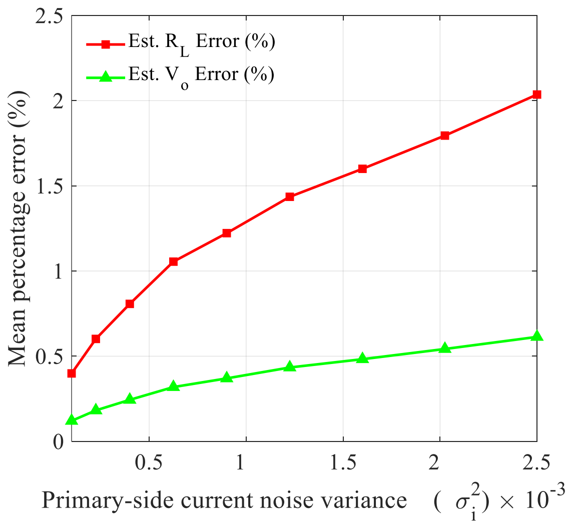

Fig. 3.4 Comparison of mean percentage errors of estimated R_L and V_o.

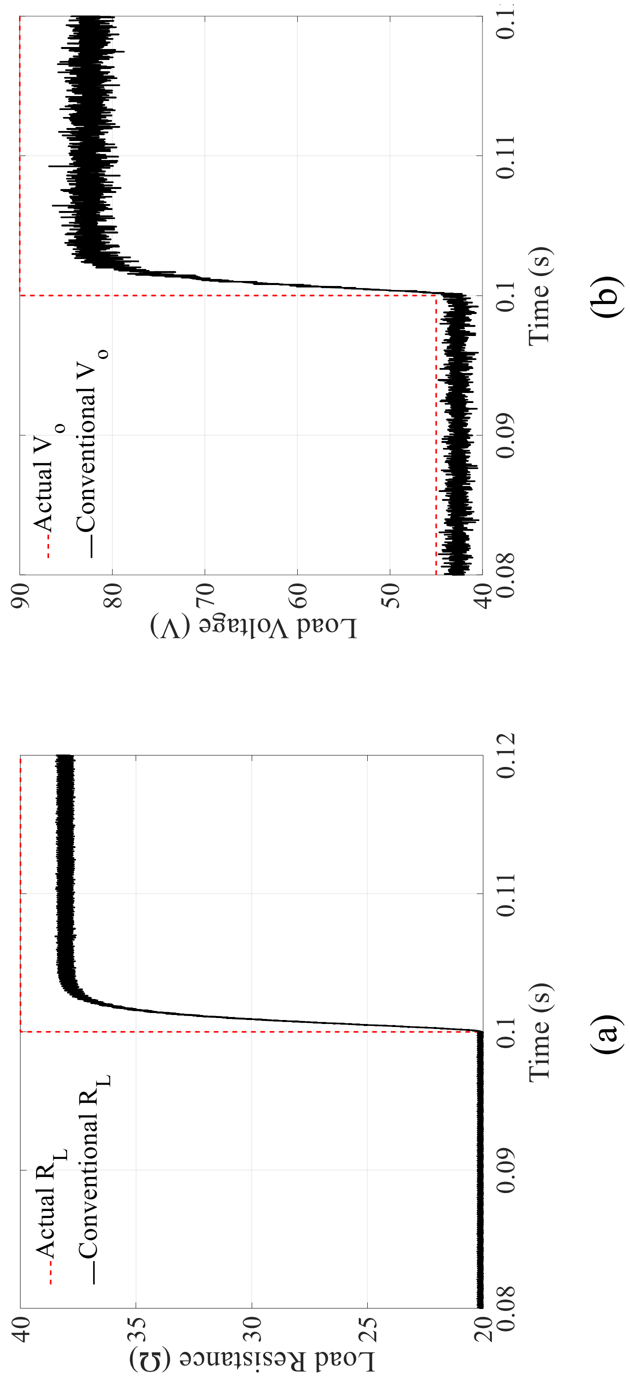

Fig. 3.5 Analytical-based conventional estimation with $\sigma^2 = 0.0025$ of (a) load resistance and (b) load voltage.

parameter identification following a load step change on the secondary-side has increased deviation error from the actual value, that is propagated in V_o which follows R_L estimation. Estimation error for R_L estimation is 0.5% and 7.1% before and after load step change, respectively, while in V_o estimation error is 2.4% and 7.9% before and after the load step change, respectively. The noise affects prior R_L identification and is amplified in subsequent V_o estimation. The estimated load parameters are erroneous in terms of reduced accuracy and sensitivity to noise.

3.3 Conclusion of the Chapter

In summary, conventional sole analytical identification method of the IWPT system without any feedback has major drawbacks. First, the conventional sole analytical method is ineffective to dynamic adaptability to system changes during dynamic operation. If variations in the load side occur during system operation, a fixed analytical solution has been demonstrated as not able to adjust flexibly and accordingly to accurately track the dynamic output parameters. Second, conventional sole analytical models are susceptible and vulnerable to noise. Since the conventional model assumes a noiseless system, any measurement noise from the sensor or uncertainty noise in the practical system can lead to propagation as well as amplification of error during identification. When sensed values are used in the model, noise in the sensed quantities will propagate through the analytical formula to the identified output parameters, being amplified in the process.

Therefore, a conventional sole analytical approach is observed to be vulnerable as it is not as accurate outside the idealized set of nominal system operation. By contrast, an identification method that is insusceptible to noise would robustly enhance the dynamic system's parameter estimation.

Chapter 4

Proposed Load Identification Utilizing Two-Step Kalman Estimator Approach

This chapter proposes an effective identification strategy that leverages the strengths of both analytical identification and a filter-based approach of Kalman estimator to identify dynamic output parameters. This analysis is under the consideration that the coupling is defined, as the transmitting and receiving platforms are under guided positioning in accordance with Qi wireless charging standards [64]. Guided positioning refers to a method of positioning the receiver on the interface surface of a transmitter base station based magnetic attraction without any moving mechanical parts whereas unguided positioning or free positioning refers to movable coil to locate the charging device as demonstrated in Fig. 4.1 [65]. This positioning enables the charging process to maintain mutual coupling by avoiding misalignment of transmitter and receiver coils.

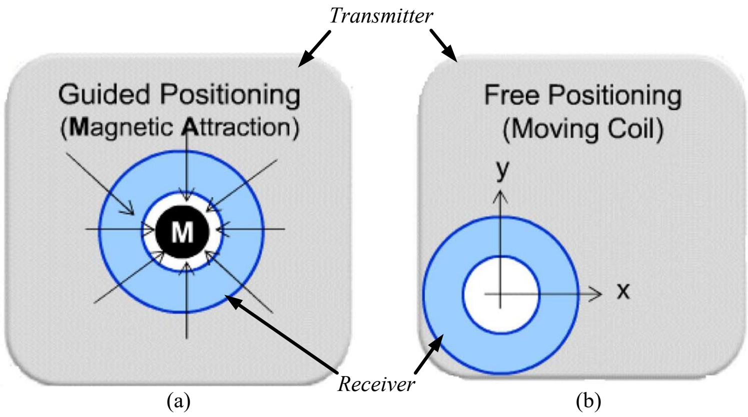

Fig. 4.1 Demonstration of (a) guided positioning and (b) unguided positioning [65].

The two-step identification strategy of an SS-compensated IWPT system proposed in this thesis is illustrated in Fig. 4.2. The first step of this strategy is to identify the equivalent load resistance R_{eq} as the baseline parameter. This quantity has been analytically recognized in the procedure provided as (3.7) in Chapter 3.

4.1 Dynamic State-Space Model and Kalman Filtering Implementation

Having successfully acquired the baseline parameter, R_{eq}, rather than to analytically estimate V_o sequentially utilizing (3.11), a Kalman estimator is adopted for the output load voltage V_o identification in the second step. To implement the Kalman estimator, a state-space representation of the system is first established. The state variables defined as

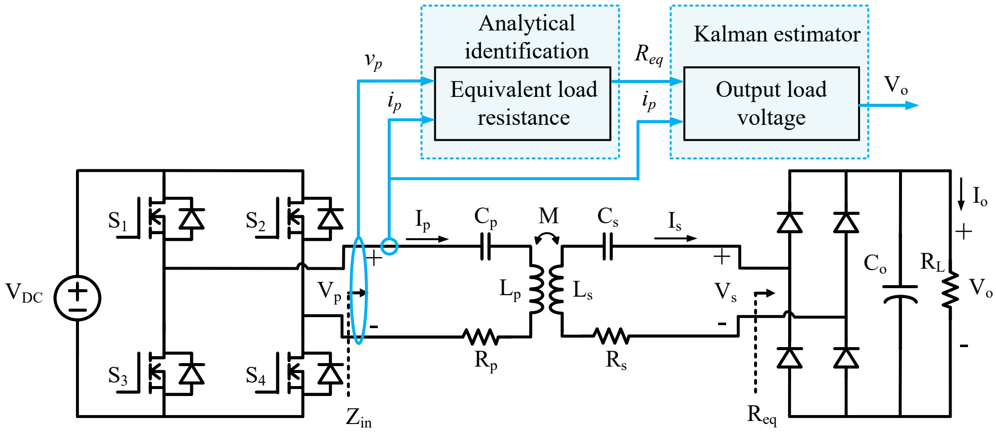

Fig. 4.2 Two-step identification of an SS-compensated IWPT system.

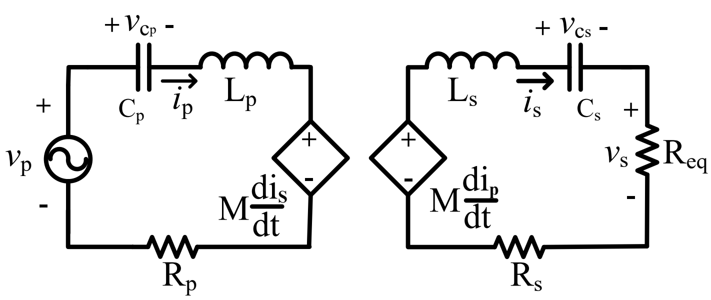

Fig. 4.3 Schematic of a magnetically coupled IWPT system.

$$\boldsymbol{X} = [x_1, x_2, x_3, x_4]^T \tag{4.1}$$

$$= \left[i_p, i_s, v_{C_p}, v_{C_s}\right]^T, \tag{4.2}$$

describe the state in the energy storage elements in the context of the equivalent circuit of this IWPT system. From Fig. 4.3 which illustrates a magnetically coupled IWPT system with mutual inductance modelled as current-dependent voltage sources and v_p described as input u, KVL application produces the following state equations:

$$M\dot{x_1} = R_{eq}x_2 + L_s\dot{x_2} + R_s x_2 + x_4, \tag{4.3}$$

$$u = x_3 + R_p x_1 + L_p\dot{x_1} + M\dot{x_2}, \tag{4.4}$$

$$\dot{x_3} = \frac{1}{C_p}x_1, \tag{4.5}$$

$$\dot{x_4} = \frac{1}{C_s}x_2. \tag{4.6}$$

Solving for the state-space equations, first the two KVLs of the primary-side and secondary-side in Fig. 4.3 are put in 2×2 matrix form

$$\begin{bmatrix} L_p & M \\ M & L_s \end{bmatrix} \begin{bmatrix} \dot{x_1} \\ \dot{x_2} \end{bmatrix} = \begin{bmatrix} u - R_p x_1 - x_3 \\ -(R_s + R_{eq})x_2 - x_4 \end{bmatrix}. \tag{4.7}$$

Inverting the 2×2 system then gives $\dot{x_1}$ and $\dot{x_2}$ as

$$\begin{bmatrix} \dot{x_1} \\ \dot{x_2} \end{bmatrix} = \frac{1}{L_i} \begin{bmatrix} L_s & -M \\ -M & L_p \end{bmatrix} \begin{bmatrix} u - R_p x_1 - x_3 \\ -(R_s + R_{eq}) x_2 - x_4 \end{bmatrix},$$

where

$$L_i = L_p L_s - M^2 \tag{4.8}$$

term assumes imperfect coupling. Expanding, this two state equations become

$$\dot{x_1} = \frac{L_s}{L_i} u - \frac{R_p L_s}{L_i} x_1 + \frac{M(R_s + R_{eq})}{L_i} x_2 - \frac{L_s}{L_i} x_3 + \frac{M}{L_i} x_4, \tag{4.9}$$

$$\dot{x_2} = -\frac{M}{L_i} u + \frac{R_p M}{L_i} x_1 - \frac{L_p(R_s + R_{eq})}{L_i} x_2 + \frac{M}{L_i} x_3 - \frac{L_p}{L_i} x_4. \tag{4.10}$$

Now, including state equations (4.5) and (4.6), collect into state transition matrix A, input matrix B, output matrix C and direct transition matrix D, that model the dynamic behaviour of the IWPT system. These matrices are

$$A = \begin{bmatrix} \frac{-R_p L_s}{L_i} & \frac{M\left(R_s + R_{eq}\right)}{L_i} & \frac{-L_s}{L_i} & \frac{M}{L_i} \\ \frac{R_p M}{L_i} & \frac{-L_p\left(R_s + R_{eq}\right)}{L_i} & \frac{M}{L_i} & \frac{-L_p}{L_i} \\ \frac{1}{C_p} & 0 & 0 & 0 \\ 0 & \frac{1}{C_s} & 0 & 0 \end{bmatrix} \tag{4.11}$$

$$B = \begin{bmatrix} \frac{L_s}{L_i} & \frac{-M}{L_i} & 0 & 0 \end{bmatrix}^T \tag{4.12}$$

$$C = \begin{bmatrix} 1 & 0 & 0 & 0 \end{bmatrix} \tag{4.13}$$

$$D = \begin{bmatrix} 0 \end{bmatrix}. \tag{4.14}$$

The continuous time model state space representation is

$$\dot{\boldsymbol{x}}(t) = A\boldsymbol{x}(t) + B\boldsymbol{u}(t) + w(t), \tag{4.15}$$

$$\boldsymbol{z}(t) = C\boldsymbol{x}(t) + D\boldsymbol{u}(t) + v(t), \tag{4.16}$$

where $w(t)$ is the process noise and $v(t)$ is the measurement noise. To implement the Kalman filter estimator, forward Euler's method [66] is applied to obtain a discrete model of the system as

$$\dot{\boldsymbol{x}}(t) \approx \frac{\boldsymbol{x}(k) - \boldsymbol{x}(k-1)}{T_s}, \tag{4.17}$$

where k refers to the iteration index and T_s is the sampling time. Substituting and solving for the state space representation,

$$\boldsymbol{x}(k) = (\boldsymbol{I} + AT_s)\boldsymbol{x}(k-1) + BT_s\boldsymbol{x}(k-1) + w(k-1), \tag{4.18}$$

$$\boldsymbol{z}(k-1) = C\boldsymbol{x}(k-1) + D(k)\boldsymbol{u}(k-1) + v(k-1), \tag{4.19}$$

where discretized matrices $A_d = (\boldsymbol{I} + AT_s)$ and $B_d = BT_s$ are

$$A_d = \begin{bmatrix} 1 - \frac{-R_p L_s}{L_i} T_s & \frac{M\left(R_s + R_{eq}\right)}{L_i} T_s & \frac{-L_s}{L_i} T_s & \frac{M}{L_i} T_s \\ \frac{R_p M}{L_i} T_s & 1 - \frac{-L_p\left(R_s + R_{eq}\right)}{L_i} T_s & \frac{M}{L_i} T_s & \frac{-L_p}{L_i} T_s \\ \frac{1}{C_p} T_s & 0 & 1 & 0 \\ 0 & \frac{1}{C_s} T_s & 0 & 1 \end{bmatrix}, \tag{4.20}$$

$$B_d = \begin{bmatrix} \frac{L_s}{L_i}T_s & \frac{-M}{L_i}T_s & 0 & 0 \end{bmatrix}^T. \tag{4.21}$$

Hence, the discretized model is

$$\boldsymbol{x}(k) = A_d\boldsymbol{x}(k-1) + B_d\boldsymbol{u}(k-1) + w(k-1), \tag{4.22}$$

$$\boldsymbol{z}(k-1) = C\boldsymbol{x}(k-1) + D(k)\boldsymbol{u}(k-1) + v(k-1), \tag{4.23}$$

where $\boldsymbol{x}(k)$ is the four-by-one state vector which in this case is $\boldsymbol{x}(k)$=$[x_1\ x_2\ x_3\ x_4]^T$, and $\boldsymbol{z}(k)$ is the one-by-one observation vector that corresponds to observation matrix C of the state of $\boldsymbol{x}(k)$.

Since i_s is obtained from output result of $\boldsymbol{z}(k)$ and R_{eq} has already been identified, the output DC voltage V_o

$$V_o = \frac{\pi}{2\sqrt{2}}R_{eq}\boldsymbol{z}(k), \tag{4.24}$$

is achieved after the lossless full bridge rectification in (4.24). The Kalman estimator operates in two phases of prediction and correction [67] as follows:

1) prediction (time update)

$$\hat{\boldsymbol{x}}(k|k-1) = A_d\hat{\boldsymbol{x}}(k-1|k-1) + B_d\boldsymbol{u}(k-1), \tag{4.25}$$

$$\boldsymbol{P}(k|k-1) = A_d\boldsymbol{P}(k-1|k-1)A_d^T + Q(k), \tag{4.26}$$

2) correction (measurement update)

$$\boldsymbol{K}(k) = \boldsymbol{P}(k|k-1)C^T(k)\left(C(k)\boldsymbol{P}(k|k-1)C^T(k) + R(k)\right)^{-1}, \tag{4.27}$$

$$\hat{\boldsymbol{x}}(k|k) = \hat{\boldsymbol{x}}(k|k-1) + \boldsymbol{K}(k)\left(\boldsymbol{z}(k) - C(k)\hat{\boldsymbol{x}}(k|k-1)\right), \tag{4.28}$$

$$\boldsymbol{P}(k|k) = \left(I - \boldsymbol{K}(k)C(k)\right)\boldsymbol{P}(k|k-1). \tag{4.29}$$

In this Kalman operation, $\boldsymbol{P}(k)$ is the covariance matrix that measures the estimated accuracy of the state estimate and $\boldsymbol{K}(k)$ is the Kalman gain that optimally balances the trust between the prediction of the system model and the incoming sensor measurements. Here, a high gain places more trust in the measurement while a low gain favors the prediction. $Q(k)$ and $R(k)$ are noise covariance matrices from the uncertainty of the dynamic system model and measurements obtained through sensors, respectively.

The adaptive update mechanism of the Kalman estimator thereby enhances robustness to noise and load variations. By recursively minimizing the posteriori covariance, the Kalman estimator inherently minimizes random measurement noise [67] while remaining responsive to system load changes through effectively linearizing the nonlinear dynamics of the system for accurate tracking. As a result, the estimated output load voltage stays stable under sensor jitters, yet rapidly tracks the actual shifts in the dynamic load. This robustness helps to improve voltage tracking accuracy by adapting $\boldsymbol{P}(k)$ and $\boldsymbol{K}(k)$ at each step of the prediction and correction phases.

Computational speed is of importance as well when it comes to real-time implementation of an identification technique. In regards to the case of load variation in the dynamic IWPT system, the time for executing the identification algorithm will depend on the complexity of the estimation process. The estimator depends on the number of floating point operations required and the number of tasks a processor can handle within a specified period. Calculation of the computation time is done by taking the product of the floating point operations performed per second and the clock speed which is 200MHz for TMS320F28379D [68] digital signal processor (DSP). For the proposed two-step identification, approximately 481 arithmetic operations for (4.20)-(4.23) are executed.

Therefore, assuming 200 million floating point operations per second the estimation computation time is 481x(1/200,000,000) $\approx$ 0.002405 s. For the sole analytical-based conventional identification comprising of approximately 167 arithmetic operations performed for (3.7)-(3.11), the computation time for the estimation is 167x(1/200,000,000) $\approx$ 0.000835 s. A trade-off of the proposed identification approach is that the computation time is noted to be longer compared to the conventional method due to the composition of matrices as summarized in Table 4.1.

Table 4.1 Comparison of computation time.

Identification method	Operations	Computation
Conventional analytical method	167	0.000835 s
Proposed identification	481	0.002405 s

4.2 Digital Phase Detector Finite-State-Machine Implementation

The prior assumption has been that the system is at or close to resonance. Now the system needs to be considered for the cases that the system operation deviates due to non-resistive reflected impedance which are bound to occur in a practical real-world IWPT system. At this off-resonance states, the angle θ of the phase between primary-side voltage and voltage and current is required to carry out the identification of the unknown parameters.

To obtain this, a digital phase detector finite-state-machine (FSM) is implemented as illustrated in Fig. 4.4. Voltage and current signals are acquired from the primary-side of the IWPT system and passed through zero-crossing comparators where ref is zero reference signal. The up-down output signals of both voltage and current are fed into the TMS320F28379D through designated general-purpose input/output (GPIO) pins. Here, depending on the current state and the input received, the FSM outputs a value of angle θ between the voltage and current with polarity to indicate leading or lagging depending on the captured zero-crossing time of both signals. This is then used to calculate real and imaginary impedance parts in (3.12) and (3.13), respectively, for the equivalent load resistance identification in (3.7).

The information that needs to be extracted is whether the current is leading the voltage or voltage is leading the current, and if so by how much. Fig. 4.5 demonstrates the finite state machine where S is the input signal. Lets consider that t_i is the zero-crossing time of the primary-side current signal and t_v is the zero-crossing time of the primary-side voltage signal. If the primary-side current leads, $S = 1$ and the state is 1 to show that the impedance is capacitive,

$$t_i - t_v < 0 : S \rightarrow 1. \tag{4.30}$$

If the primary-side current lags primary-side voltage, $S = 0$ and the state is -1 to represent inductive impedance,

$$t_i - t_v > 0 : S \rightarrow 0. \tag{4.31}$$

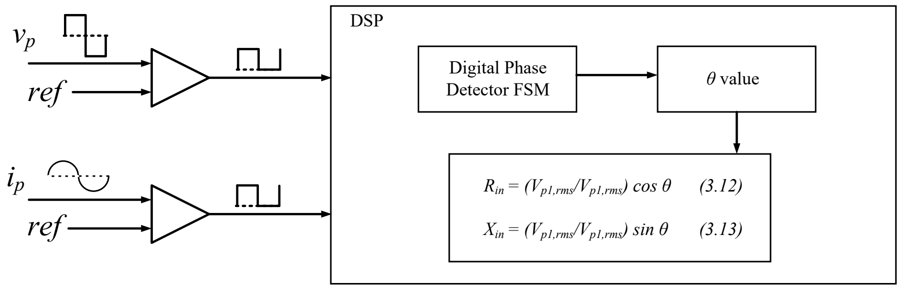

Fig. 4.4 Digital phase detector implementation.

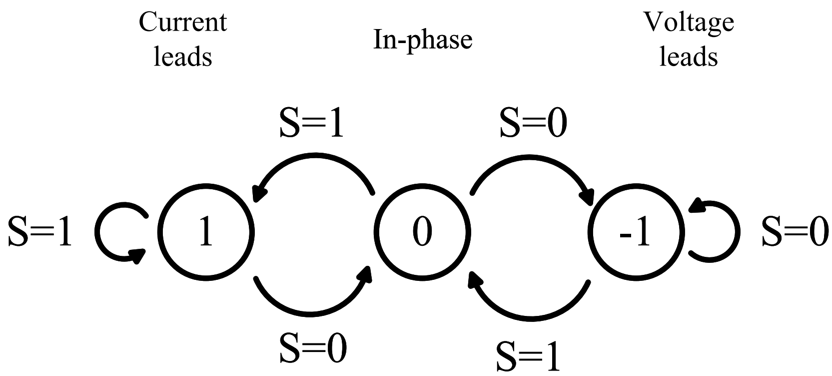

Fig. 4.5 Finite-state machine implementation.

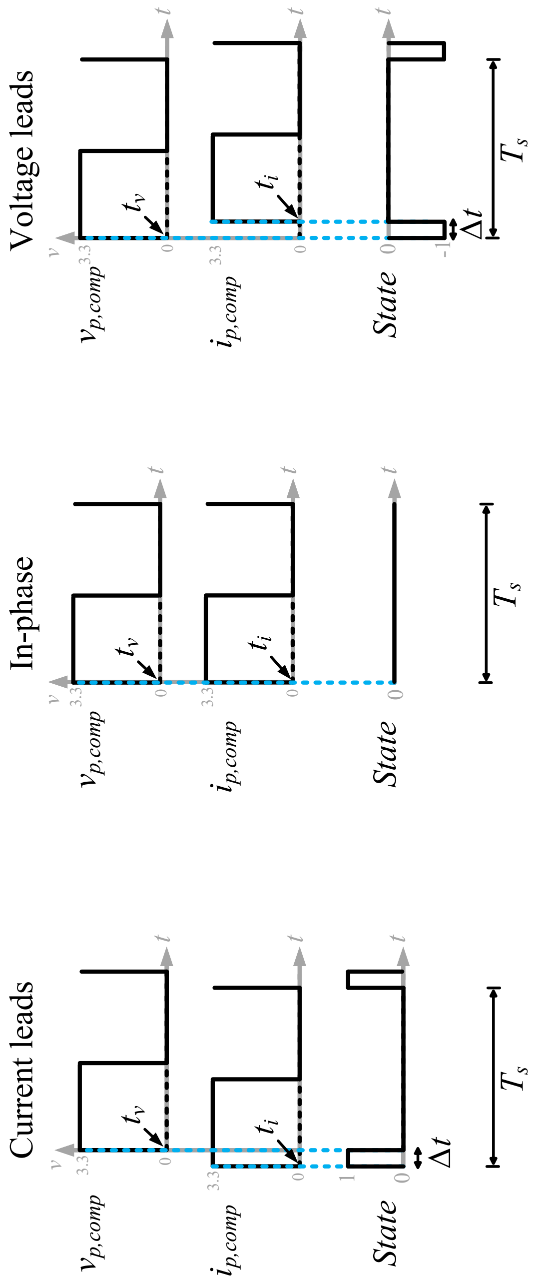

Fig. 4.6 Comparator outputs comparison.

When the primary-side current and primary-side voltage are in-phase, the state is 0 for resistive reflected impedance,

$$t_i - t_v = 0 : S \rightarrow 0. \tag{4.32}$$

Fig. 4.6 shows an illustration of the described process. $v_{p,comp}$ and $i_{p,comp}$ are the comparator output signals fed into the phase detector in the DSP . The time difference Δt between the primary-side current and primary-side voltage signals then provides the value of the angle θ as

$$\theta = \frac{\Delta t}{T_s} 360^0 \tag{4.33}$$

where T_s is the switching period of the system, corresponding inversely to the switching frequency.

4.3 Conclusion of the Chapter

In summary, the proposed two-step identification method strategically decouples the nonlinear IWPT system to be estimated. The primary goal of the first step is to provide the identified baseline value of the unknown AC load resistance parameter to be utilized for the linear state-space transition matrix A. Subsequently, second step employs a linear Kalman estimator model whose superior ability is to handle measurement and system process noise as well as track dynamic load voltage changes. Also, a phase detector finite state machine is discussed and implemented to determine the phase angle value between the primary-side quantities of voltage and current.

Chapter 5

Verification

In this chapter, verifications are carried out. The verifications proceeds to test the performance of the proposed two-step identification approach discussed in Chapter 4. These are performed via software simulations as well as using a hardware test-bench. This done is to check the feasibility of this proposed identification method in a practical non-ideal IWPT system.

5.1 Simulation Verification

Simulation of a SS-compensated IWPT system is conducted in PSIM software [69] as shown by the simulation schematic in Fig. 5.1 to verify the two-step identification approach utilizing the specification parameters in Table 3.1. Also, to account for noise in the simulation, Fig. 5.2 shows AWGN that is injected into the simulation to imitate practical current sensor that has inherent measurement noise. In the probability distribution plot of the injected noise amplitudes, shown in Fig. 5.3 of the probability density function (PDF), standard deviation (σ) is set between 0.01 and 0.05, corresponding to nominal noise levels of 1% to 5% of the

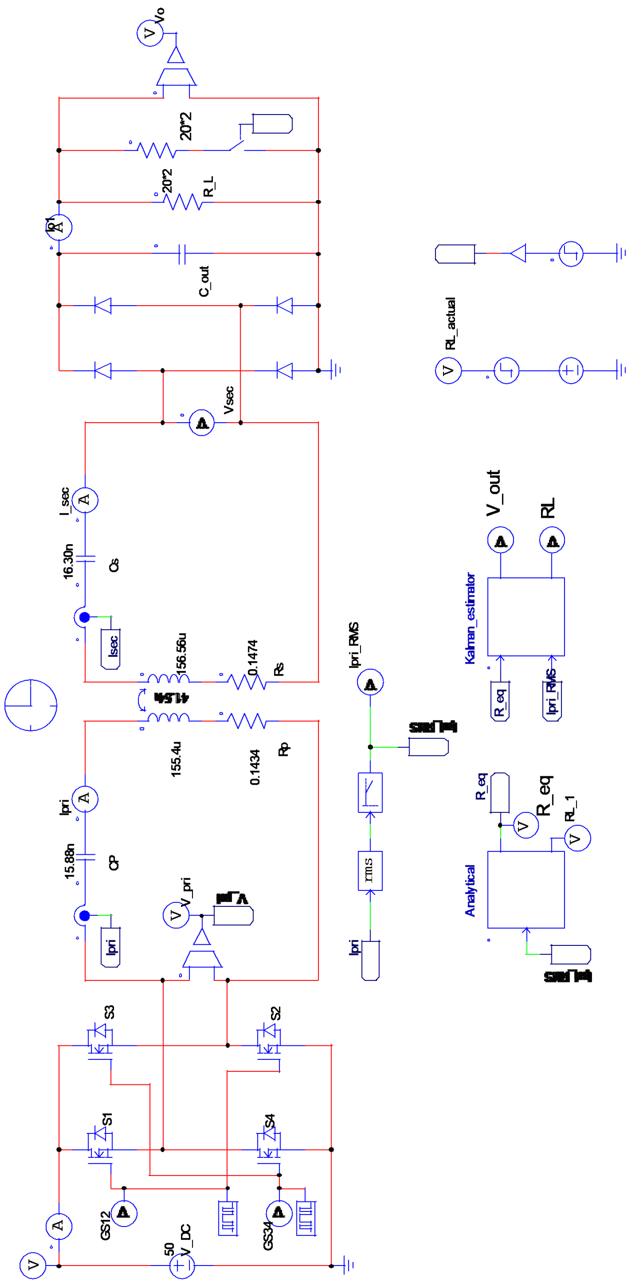

Fig. 5.1 Simulation circuit schematic.

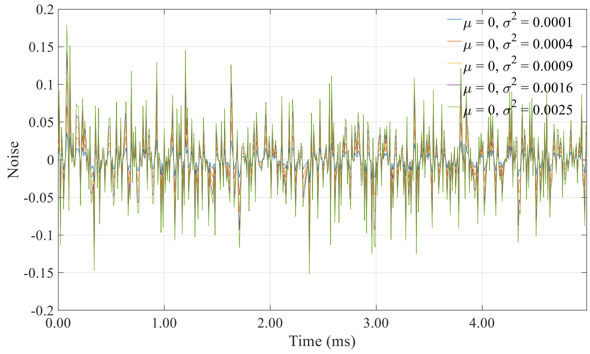

Fig. 5.2 Additive White Gaussian noise injected into the sensed current.

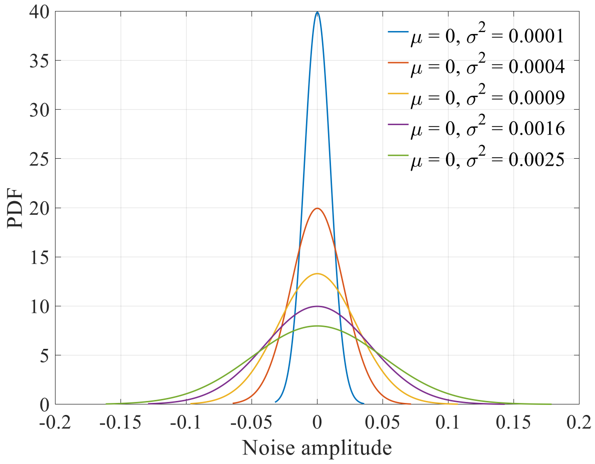

Fig. 5.3 Probability distribution of noise amplitude.

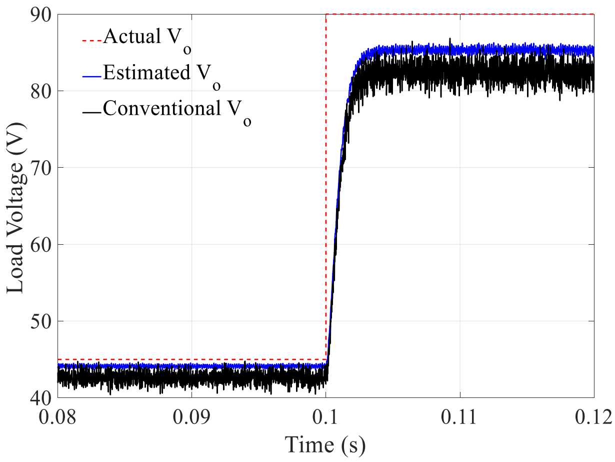

Fig. 5.4 Simulation result with load step change for output voltage estimation.

measured value. Interpreted statistically, approximately 68% of the noisy measurements do lie within $\pm\sigma$, and about 95% lie within $\pm 2\sigma$ of the true value. A value of $\sigma = 0.05$ is chosen to emulate a worst-case scenario, where the sensor exhibits relatively high variability, that is, upto ±5% for one standard deviation in its acquired measurements. This noise is injected into the PSIM system simulation via the C-block code function shown in (Appendix) using a Box–Muller transformation which is a pseudo-random number sampling method for generating pairs of independent, standard, normally distributed (zero expectation, unit variance) random numbers [70]. This is employed to provide an algorithm for transformation to the desired probability distribution. Also, the noise covariance parameters of Q_k and R_k for tuning the behavior of the filter in this simulation are set as

$$Q(k) = \begin{bmatrix} 0.03 & 0 & 0 & 0 \\ 0 & 0.03 & 0 & 0 \\ 0 & 0 & 0.03 & 0 \\ 0 & 0 & 0 & 0.03 \end{bmatrix}, \tag{5.1}$$

$$R(k) = 10^{-8}. \tag{5.2}$$

Fig. 5.4 illustrates the estimate for the output voltage when disturbance is introduced for the load resistance parameter value to observe the performance of the two-step identification. From the simulation plot, the two-step identification with Kalman estimator achieves steady-state errors of 1.8 % and 4.6 % before and after the load step change, respectively, while a 7.9 % error deviation is observed for the conventional analytical identification. The Kalman estimator is seen to be immune to the sensed noise as well as propagated noise in the output voltage estimation. The limitation of sole analytical method to change in system dynamics is observed.

Theoretically, the estimation error in Chapter 3 Fig. 3.4 and the estimation error from the system verification are observed to be different with simulation verification outcome seen higher for the estimated load resistance and output load voltage as seen in Fig. 5.4. This difference is attributed to by the fundamental harmonic approximation assumption in the analytical method procedure, while the system circuit simulation contains minor harmonics content from the inverter switching during operation which compounds minute error that is not in the theoretical equation. Hence, even though the verification error obtained is not as purely theoretical, the trend of the identification error propagation is observed in the system.

Overall, the proposed two-step estimation approach improves performance for load parameter identification in dynamic conditions since the Kalman estimator adaptively filters noise and tracks dynamic changes with minimized error.

5.2 Hardware Test-bench Setup

An experimental hardware testing platform for a 75 W IWPT with 50V input and 40V output is setup as shown in Fig. 5.5 to evaluate the proposed identification method using the specifications provided in Table 3.1. The primary-side power source (ITECH IT-M3413) is a bidirectional DC power supply. This supply feeds a full-bridge inverter stage that utilizes high-performance power MOSFETs (CREE C3M0065100K, Silicon Carbide (SiC)) that are suitable for high-frequency applications.

The transmitter and receiver coils are constructed using 3.5mm diameter Litz wire to mitigate skin and proximity effects at high frequencies. The primary coil has an inner radius of 130.7 mm and an outer radius of 175.8 mm, while the secondary coil has an inner radius of 126.9 mm and an outer radius of 171.0 mm. For this study, the coils were maintained

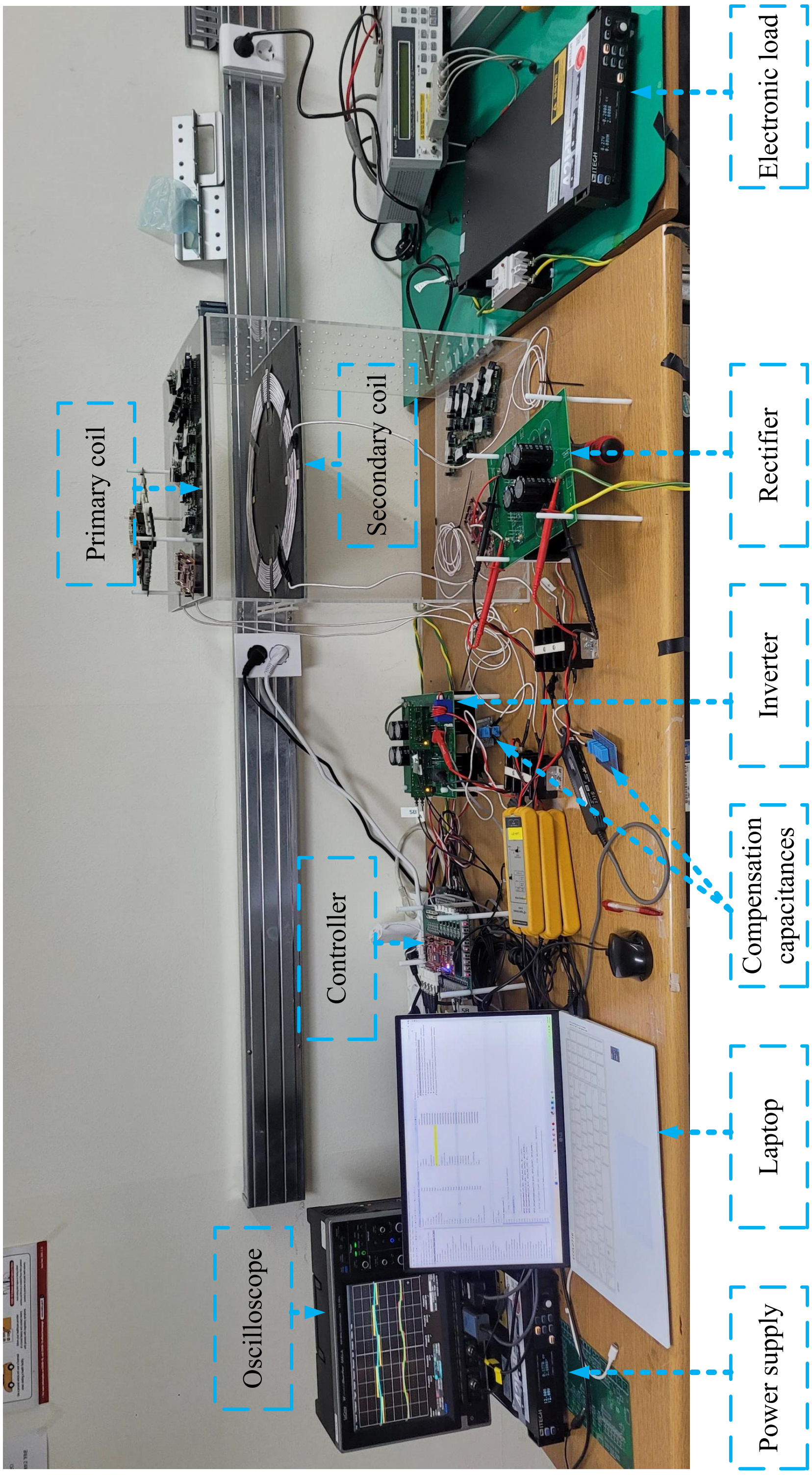

Fig. 5.5 Experimental hardware setup.

at a separation distance of 130.4 mm which provide a mutual inductance value of 41.54 μH. These loop coils are mounted on 40mm by 40mm ferrite square plates on both sides to provide magnetic flux shaping and shielding. On the secondary-side, a full-wave rectifier is implemented using Schottky diodes (CREE C3D16060, SiC) and a DC electronic load serves as a variable load for this testing purpose.

A current sensor (LEM LA 55-P) is used to obtain current readings of the primary-side. Differential probes (SI-9002) and current probes (LeCroy CP030) are used to measure voltage and current waveforms, respectively, onto the oscilloscope (LeCroy WaveSurfer 64Xs-A). The parameter identification is implemented by utilizing microcontroller unit (MCU) (Texas Instruments TMS320F28379D) [68]. Sensed current signal is fed into the MCU via configured 12-bit analog-to-digital conversion (ADC). The identified parameters are then converted analog output signals of the MCU using 12-bit digital-to-analog converter (DAC) whose output conversion value of V_{DAC} is [71]

$$V_{DAC} = V_{ref}\frac{D}{2^n}, \tag{5.3}$$

where V_{ref} is the reference voltage which in this setup is 5 V, D is the digital code decimal value, n is the number of bits (resolution) used to quantify the output and 2^n is the total combination which for 12-bit resolution is 4096.

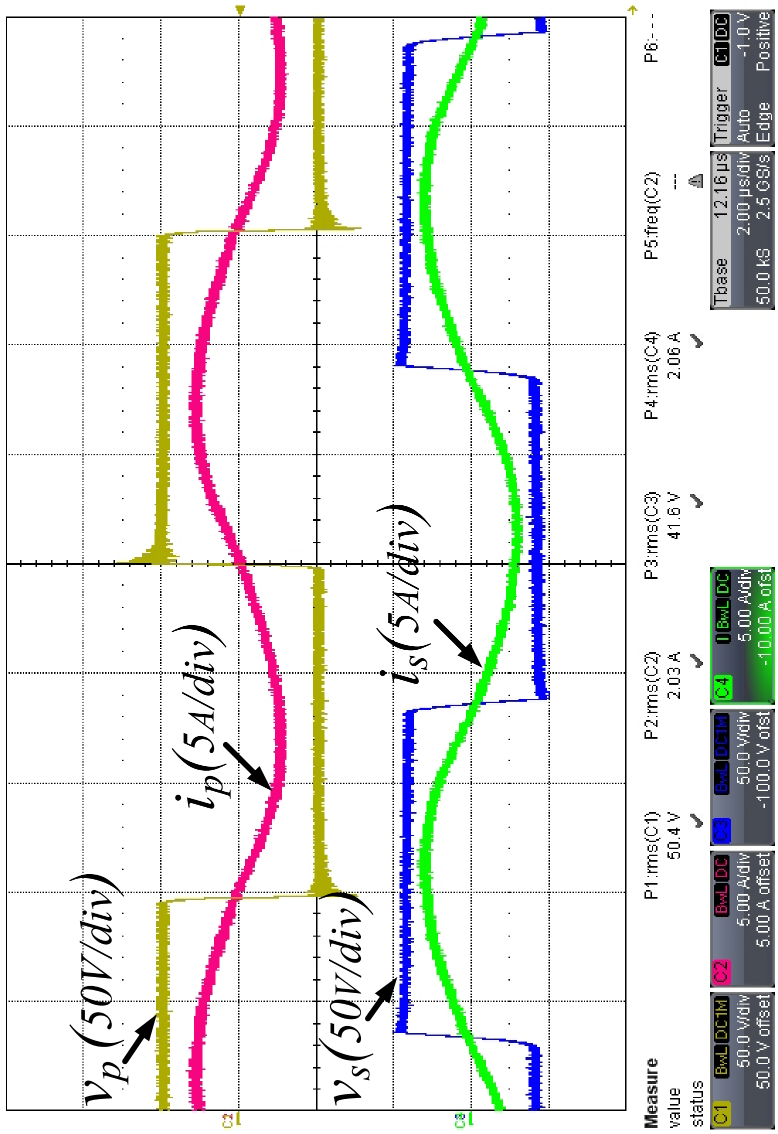

Fig. 5.6 Experimental waveform of the SS-compensated IWPT.

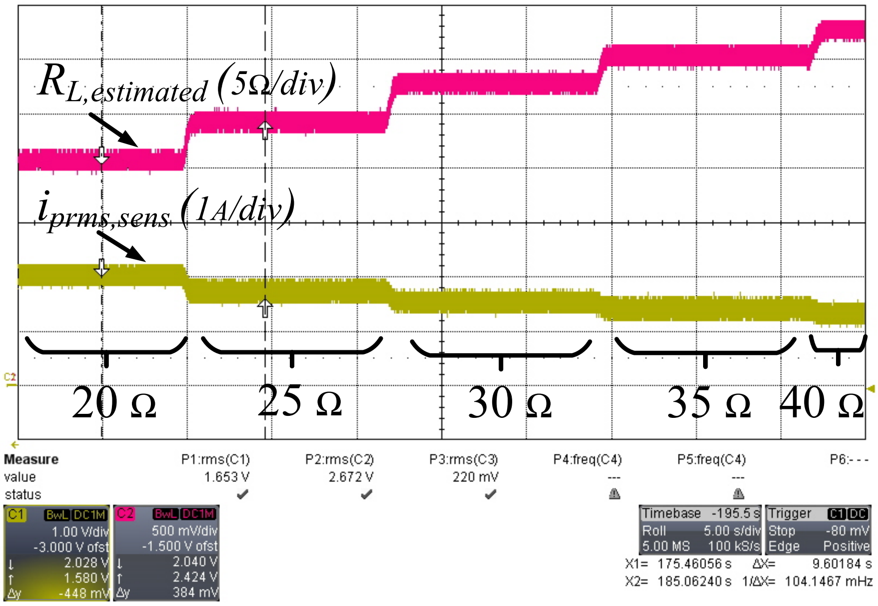

Fig. 5.7 Load resistance estimation.

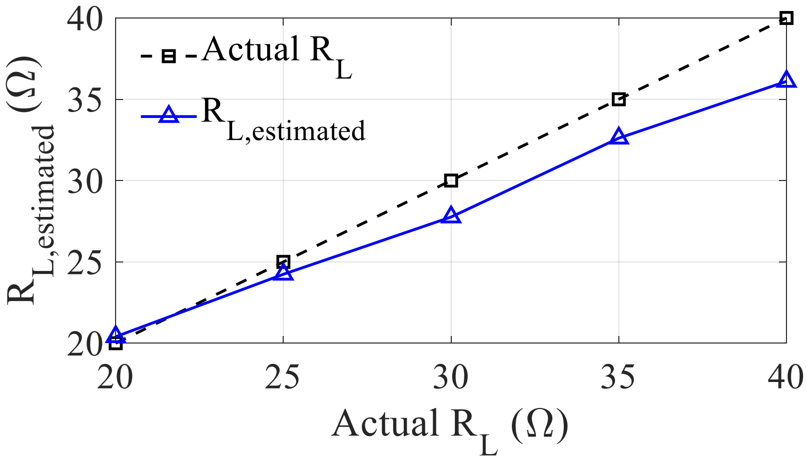

Fig. 5.8 Comparison of estimated load resistance.

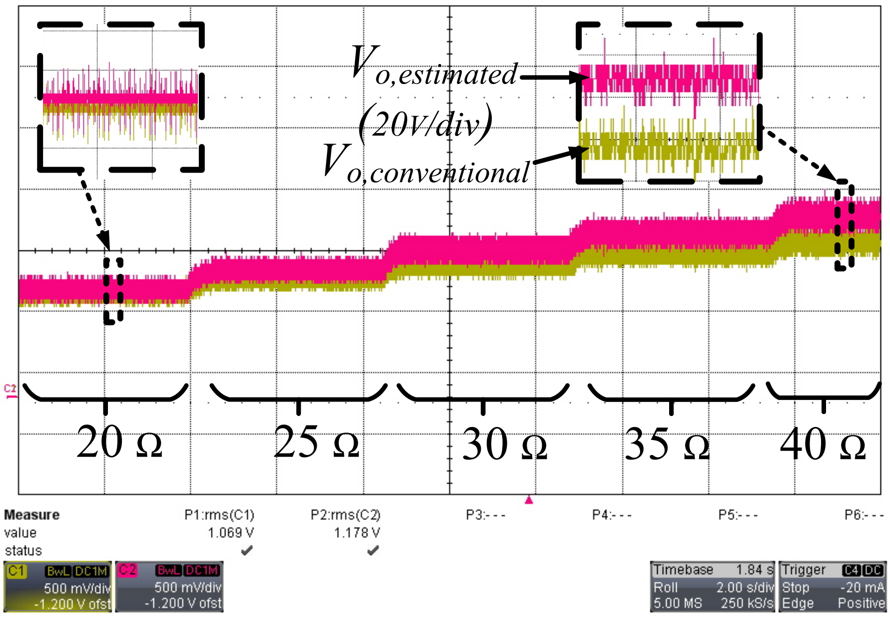

Fig. 5.9 Output load voltage estimation comparison.

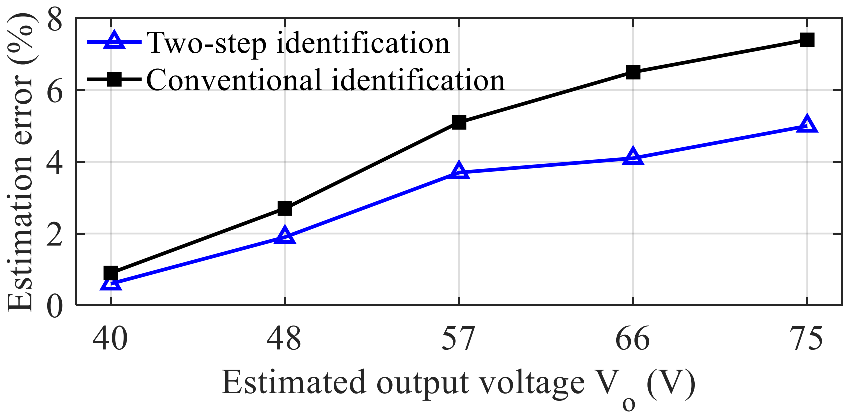

Fig. 5.10 Voltage estimation error comparison.

5.3 Test Cases for Tuned and Detuned System

5.3.1 Tuned System case

Fig. 5.6 displays the experimental waveforms of the inverter and the rectifier of the IWPT system setup in Fig. 5.5. The i_p slightly lags v_p, which indicates the desired inductive input impedance for achieving Zero Voltage Switching (ZVS) and minimizing inverter switching losses. On the secondary side, the voltage v_s and current i_s are in phase, signifying that the secondary presents a purely resistive load, ensuring efficient real power delivery.

Fig. 5.7 shows the load resistance identification obtained analytically under dynamic nominal system operation with varying load resistance. For observability within the DAC range [71], the output is transformed by 10:1 ratio. As the load resistance is gradually increased, dynamic estimation of R_L is also observed in real time. R_L is varied from 20 Ω to 40 Ω. At nominal 20 Ω, the estimated R_L is has about 1 % error and at 40 Ω the estimation error increases to about 6.9 %. It can also be seen that with increasing load resistance, the primary-side rms current decreases gradually as well, which decreases the current sensing accuracy thus affecting the estimation of R_L. As such, the best identification with least errors occurs when R_L is between 20 Ω and 25 Ω. Fig. 5.8 demonstrates the deviation trend of the estimated load resistance. Similar to the simulated outcome of the estimated load resistance, the $R_{L,estimate}$ is able to follow the actual load resistance value with about 6.9 % deviation at the maximum load resistance variation range of 40 Ω.

Fig. 5.9 shows the comparison of the estimated output load voltage V_o between the conventional sole analytical method and the proposed two-step identification method. The output voltage is plotted after computation via DAC [71]. For observability within the DAC range, the output is transformed by 40:1 ratio. At nominal voltage of 40 V the estimation is seen to have small errors in both estimation approaches. The estimation of the two-step Kalman estimator tracks 71.2 V which has approximately 5 % error while conventional estimation is 69.4 V which is approximately 7.4 % error at maximum load change. This is because with increasingly varying load resistance, the error in the prior estimated parameter of $R_{L,estimate}$ increases as well impacting output voltage estimation. This increase is illustrated with the increasingly varying load resistance in both methods in Fig. 5.10. However, the conventional method is increasingly more erroneous as it is noisy.

Compared to conventional estimation the proposed identification approach mitigates the noise as it reduces the error by approximately 32 % at maximum load resistance variation. Hence, the two-step identification proves to mitigate the noise and error as load continuously varies. Additionally, Table 5.1 shows the nominal performance comparison among conventionally proposed primary-side identification techniques for IWPT system considering several trade-offs in the implementation process.

5.3.2 Detuned System case

To test for the detuned system case, the phase detector discussed in Chapter 4 is implemented. For this, a comparator module is integrated to capture the primary-side voltage and current signals as shown on the simulation schematic of Fig. 5.11. A voltage divider is added to adjust the input voltage swing into the comparator from 50 V to within 3 V and a 3.3 V supply is connected to the pull-up resistors since open drain comparators are considered. Ground reference is given to the inverting inputs for both voltage and current comparators for zero crossing comparison. The outputs of the respective voltage and current comparators are shown on the waveform of the schematic as the desired up-down signals.

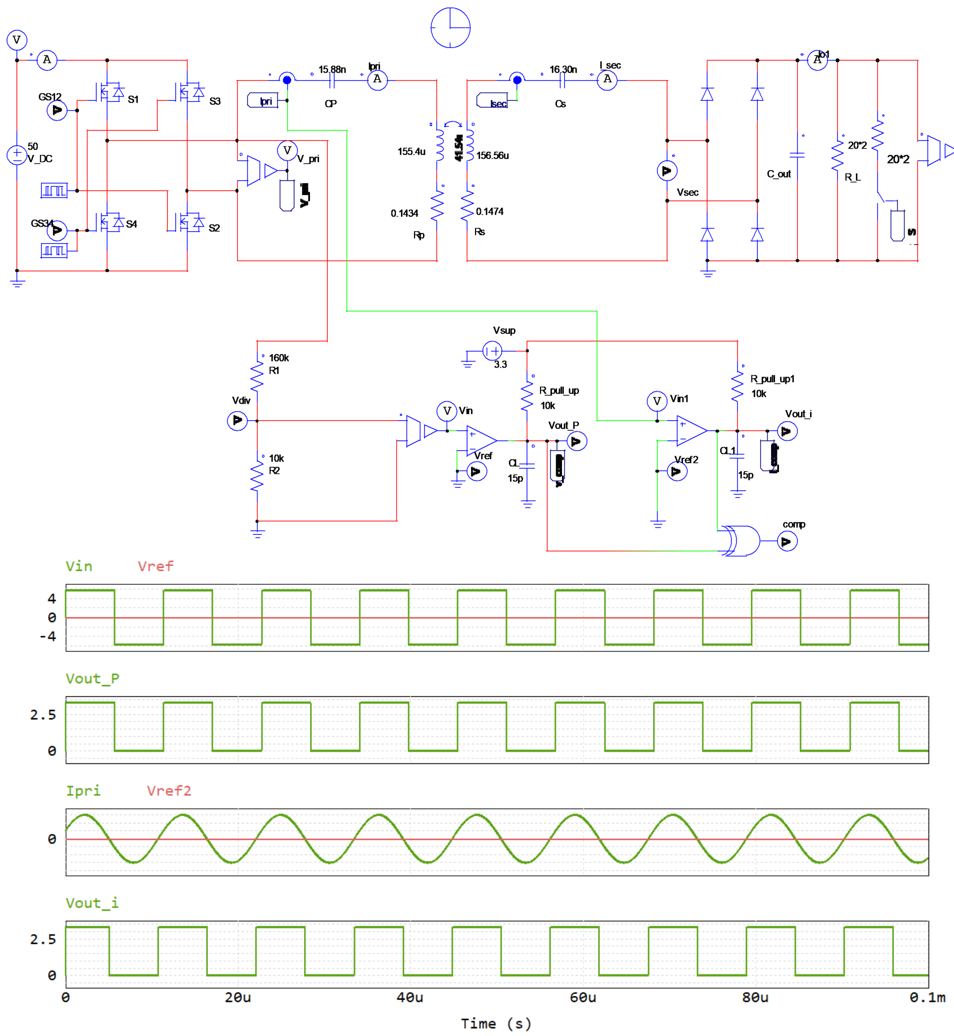

Fig. 5.11 IWPT simulation schematic with comparator module integration.

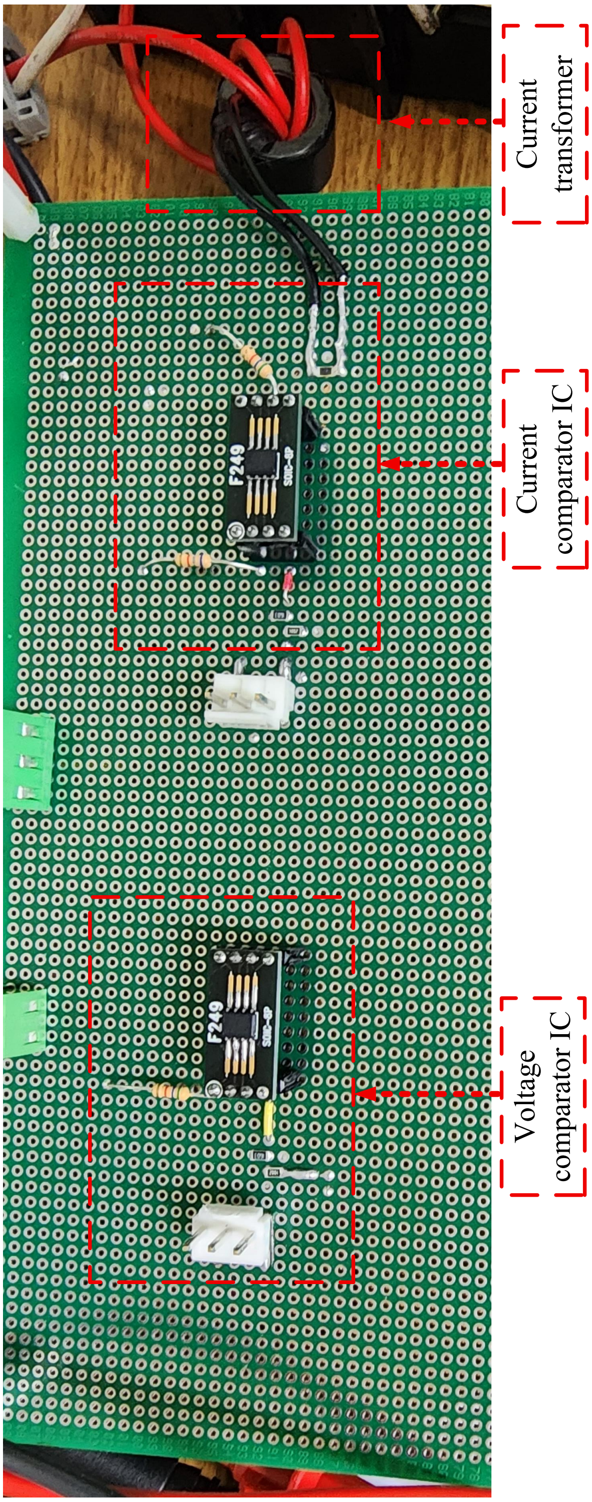

Fig. 5.12 Primary-side voltage and current comparators module.

The additional comparator module hardware is as shown in Fig. 5.12. Both current and voltage comparator integrated circuits (ICs) (Texas Instruments TLV2352) [72] are provided with 3.3 V supply and a 5.1 kΩ pull-up resistors. For the primary-side current, a ferrite core current transformer (CT) is used to safely measure the AC current. The CT is used with a 1 Ω burden and 2:5 transformation ratio for the primary-secondary windings, respectively.

Fig. 5.13 shows the primary-side voltage and primary-side current zero crossing comparator outputs. It can be seen that the up-down comparator outputs correspond to the positive zero crossing of the input voltage and current. In this figure the primary-side voltage and primary-side current are approximately 10° based on the difference of their zero crossing instants. The finite-state-machine obtains this value from the output signals of the comparator module which goes ahead to produce the phase angle for the system output voltage identification.

Comparison is shown in Fig. 5.14 of the estimated output load voltage V_o between the conventional sole analytical method and the proposed two-step identification method for off-resonance inductive case. Similar to nominal resonance case, discrepancies are minimal at nominal voltage, brief spikes at each load voltage transition and slightly larger variance at extreme loads. The estimation of the two-step Kalman estimator identifies 70.2 V with approximately 6.4 % error while conventional method estimates 68.8 V output voltage with approximately 8.2 % error at maximum load change. Compared to nominal resonance performance, the identification in this case is more erroneous as the change in voltage and current phase angle effect reduces the equivalent load resistance of the reflected impedance.

For the capacitive reflected impedance case, Fig. 5.15 shows the comparison of the estimated output load voltage V_o between the conventional sole analytical method and the proposed two-step identification. Notably, identification in this off-resonance case resembles

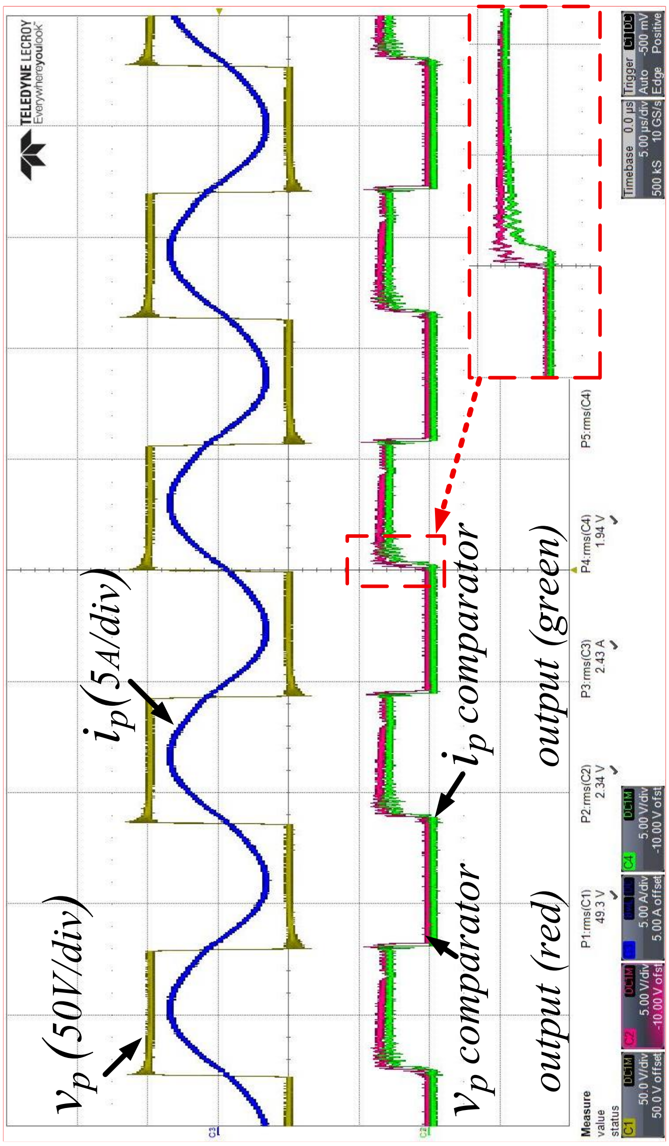

Fig. 5.13 Outputs of primary-side voltage and current comparators.

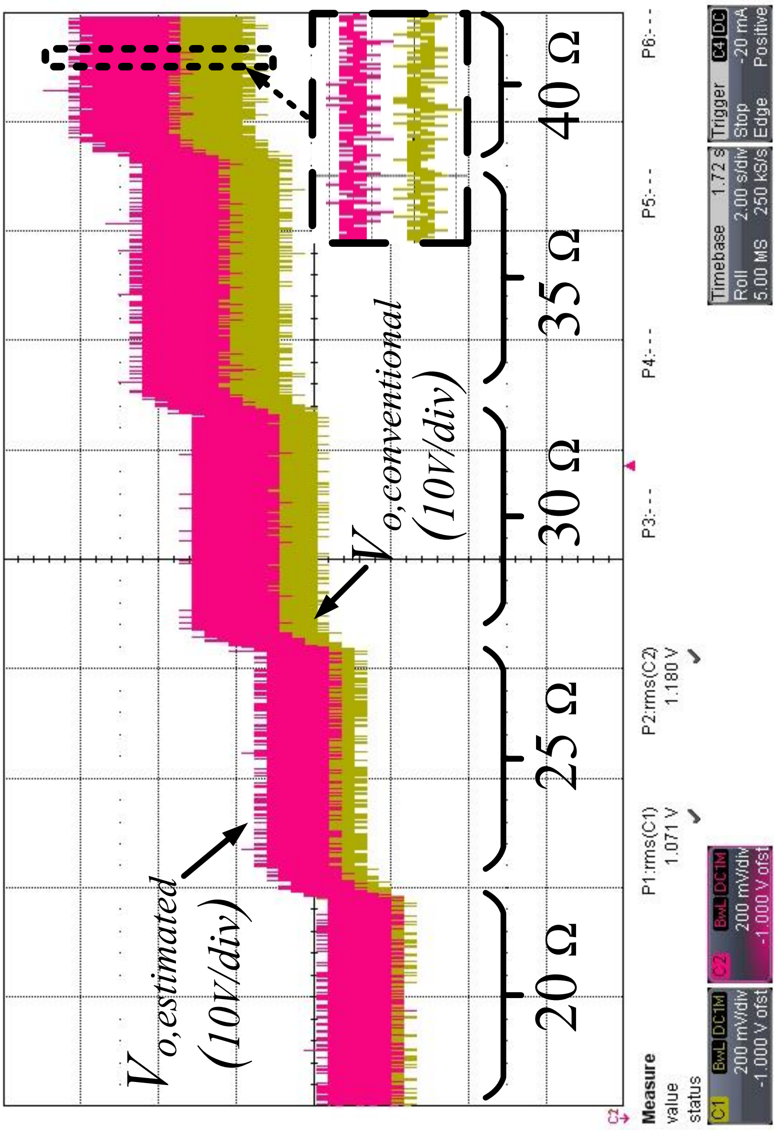

Fig. 5.14 Output load voltage estimation under inductive impedance.

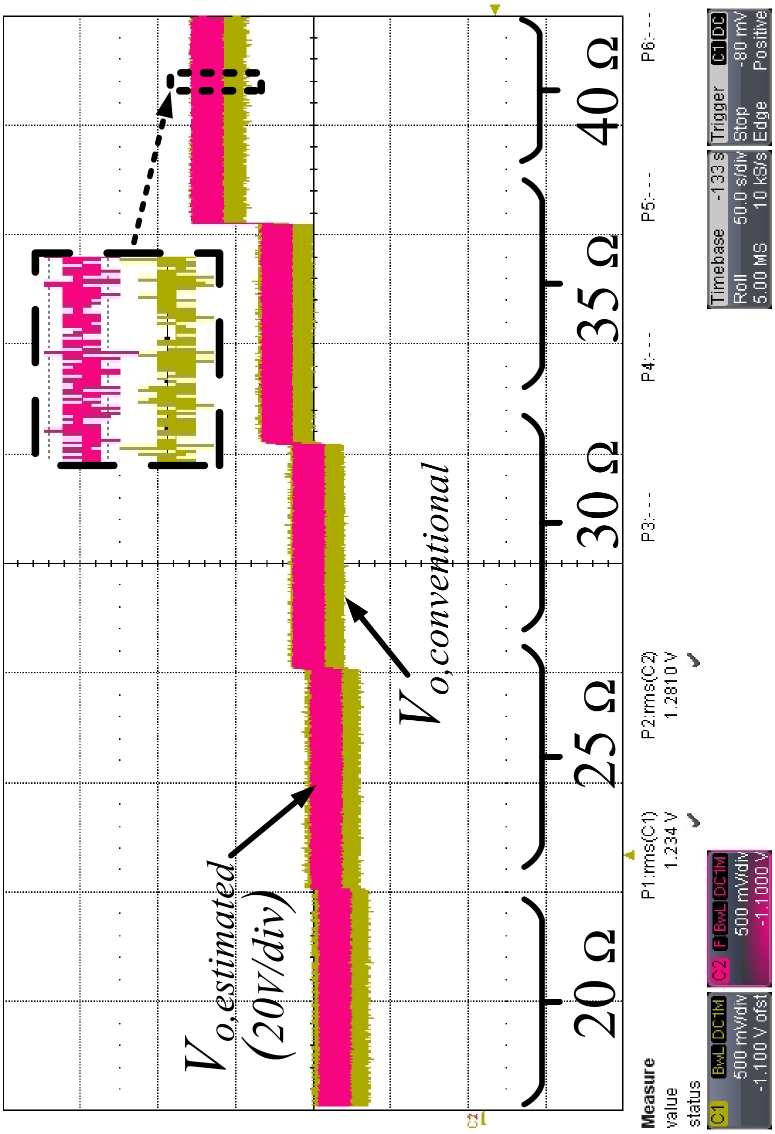

Fig. 5.15 Output load voltage estimation under capacitive impedance.

Table 5.1 Performance comparison of primary-side identification methods.

Ref.	Online Identification	Additional Hardware	Maximum Estimation Error	Computation Speed	System Complexity
[19]	X	O	< 6.6%	Not mentioned	Medium
[73]	X	O	< 1.7%	Within 8 ms	High
[74]	O	X	< 7.4%	2s	Low
[25]	O	X	< 7%	Not mentioned	Medium
[75]	O	X	< 2%	Within 10 ms	High
This work	O	X	≤ 5%	Within 3 ms	Low

Table 5.2 Comparison of load identification error for detuned system cases.

Detuned case	Conventional analytical method	Proposed identification method
Inductive resonance	8.2%	6.4%
Capacitive resonance	10.0%	8.4%

the trend observed in the nominal and inductive cases. As the load varies, the two-step estimation approach output voltage estimation occurs at 68.7 V with approximately 8.4 % error while comparably the conventional method estimates 66 V with approximately 10 % error at maximum load change. A summary of the performance comparison between the conventional analytical method and the proposed method is shown in Table 5.2. As noted, even though the IWPT system is operating at off-resonance scenarios, the tracking of the proposed two step identification is achieved more effectively.

5.4 Conclusion of the Chapter

In this chapter, the proposed identification strategy combining analytical modeling with a state-space Kalman estimator has been validated by estimating output parameters in feedback-free dynamic IWPT systems. By use the two-step identification method, it has been shown that the approach minimizes propagation of noise and tracks load variations with improved accuracy without disrupting system operation. It has been demonstrated that it significantly reduces estimation errors under noisy conditions and load changes compared to conventional sole analytical identification methods.

Chapter 6

Conclusion and Future Works

6.1 Conclusions

As discussed in this work, conventional identification methods in inductive wireless power transfer (IWPT) systems have long faced challenges in achieving accurate, stable, and real-time estimation of key secondary-side parameters using only primary-side acquired information. A state-of-the-art literature survey has explored various proposed conventional works regarding front-end identification techniques. These conventional approaches, with their simplicity and complexity trade-offs, have their limitations as they either require additional hardware, interruption of normal power transfer during system operation, or introduction of significant complex implementations, making them unsuitable for cost-sensitive or compact IWPT applications.

This thesis, therefore, presents a two-step identification strategy combining analytical modeling with a state-space Kalman estimator to identify output parameters in dynamic IWPT systems without feedback channel from the secondary-side to the primary-side. Limitation of conventional sole analytical estimation is identified where noise propagation and amplification affects the estimation output load parameters in dynamic IWPT system operation. By first deriving a baseline equivalent load resistance analytically and then applying a linear Kalman estimator dynamic model to track the output load voltage, the method minimizes propagation of noise and adapts to load variations without disrupting power transfer. Furthermore, feasibility of the proposed identification approach in off-resonance system operation scenario has been investigated by the implementation of a digital phase detector finite state machine to obtain non-resistive reflected impedance performance.

Simulation as well as experimental validations has been carried out to demonstrate significantly reduced estimation errors under noisy conditions and load changes in the system. The non-disruptive merit of this approach and its primary-side-only implementation makes it effective for real-time deployment in battery charging applications where output load varies.

6.2 Future Works

Besides the work that has been done in this thesis, more unexplored scopes can be considered to better the IWPT system. The potential topics are suggested as:

• Identification under misalignment condition of a dynamic IWPT system in addition to the proposed method.

• The sensitivity of the identification method to parameter uncertainties during system operation.

• Implementation of primary-side control technique utilizing proposed front-end identification.

• Investigation of anomaly protection mechanism in the occurrence of issues such as over-current or overheating on the secondary-side.

Biography

Andrew Ngini Mwangi was born in Nairobi, Kenya. He received his B.S. degree in electronics engineering from Hanyang University, Seoul, South Korea, in 2022. He is currently working towards the M.S. degree in electrical engineering at University of Ulsan, Ulsan, South Korea. His research interests include wireless power transfer, magnetics design and power converters.

Email: nginiandrew79@gmail.com

Journals

[1] **Andrew Ngini Mwangi** and Sung-Jin Choi, "Effective Load Identification for Inductive Wireless Power Transfer Systems Utilizing Kalman Filter Approach," **Journal of Electrical Engineering & Technology (Under review).**

[2] **Andrew Ngini Mwangi**, Chanh-Tin Truong, and Sung-Jin Choi. "Parameter Identification for Primary-Side Control of Inductive Wireless Power Transfer Systems: A Review," **IEEE Access, vol. 13, pp. 15885-15904, 2025.**

Domestic Conference

[1] **Andrew Ngini Mwangi**, Ngoc-Thao Pham, and Sung-Jin Choi, "Effective Load Identification for Inductive Wireless Power Transfer Systems Utilizing Kalman Filter Approach," **KIPE Annual Conference, 2025.**

[2] **Andrew Ngini Mwangi**, Chanh-Tin Truong, and Sung-Jin Choi, "Sensitivity Comparison of Parameter Identification Methods in Inductive Wireless Power Transfer Systems," **KIPE Annual Autumn Conference, 2024.**

[3] **Andrew Ngini Mwangi**, Chanh-Tin Truong, and Sung-Jin Choi, "Improved ZVS Criterion for Series Resonant Converters: A Simplified Approach," **KIPE Annual Conference, 2024.**

Appendix

A. Analytical estimation code

```
// PSIM C block code

#include <Stdlib.h>
#include <String.h>
#include <math.h>
#include <random>
#include <Psim.h>

#ifndef M_PI
#define M_PI 3.14159265358979323846
#endif

// GLOBAL VARIABLES
static int count = 0;
static int Ncount = 0;
static int flagSample = 1;
static double Ts ;

// Parameters
const double R_p = 0.1474;        // Ohms
const double R_s = 0.1434;        // Ohms
const double L_p = 155.4e-6;      // Henrys
const double L_s = 156.56e-6;     // Henrys
const double C_p = 15.88e-9;      // Farads
const double C_s = 16.30e-9;      // Farads
static double M = 41.547e-6;       // Henrys
static double f = 114000;          // Hz
```

```
static double Ts = 1/f;          // Hz
static double w = 2 * M_PI * f ; // rad/s
static double theta = 0.0;       // Phase angle

double V_p1_rms, I_p1_rms;
double R_in, X_in, alpha_rad;
double w_op, w_os;
double numerator_Req, denominator_Req, R_eq;
double numerator_Is1, denominator_Is1, I_s1;
double I_o, V_s1, V_o, R_L;

// Noise(AWGN) parameters
static double noise_mean  = 0.0;
static double noise_sigma = 0.05;

// Box-muller transform for noise injection
double generateGaussianNoise(double noise_mean, double noise_sigma) {
        static int haveSpare = 0;
        static double spare;
        double u, v, s;
        if (haveSpare) {
                haveSpare = 0;
                return mu + sigma * spare;
        }
        do {
                u = ((double)rand() / RAND_MAX) * 2.0 - 1.0;
                v = ((double)rand() / RAND_MAX) * 2.0 - 1.0;
                s = u*u + v*v;
        } while (s >= 1.0 || s == 0.0);
        s = sqrt(-2.0 * log(s) / s);
        spare = v * s;
        haveSpare = 1;
        return noise_mean + noise_sigma * (u * s);
}
//////////////////////////////////////////////////////////////////////
// FUNCTION: SimulationStep
// This function runs at every time step.
// strcpy(szErrorMsg, "Error message here...");
// DO NOT CHANGE THE NAME OR PARAMETERS OF THIS FUNCTION
void SimulationStep(
double t, double delt, double *in, double *out,
int *pnError, char * szErrorMsg,
void ** reserved_UserData, int reserved_ThreadIndex,
```

```
void * reserved_AppPtr)
{
        // ENTER YOUR CODE HERE...
        // Calculate the no. of counts in one period
        Ncount = Ts / delt;

        // Check if the counter reaches end of the period. If yes,
        // set the sampling flag to 1.
        if (count >= Ncount) {
                flagSample = 1;
                //      Reset the counter to 0.
                count = 0;
        }

        // If the sampling flag is 1, sample the inputs

        if (flagSample == 1) {
                //              Reset the sampling flag
                flagSample = 0;

        if (t >= 1e-3) {

        V_p1_rms = 50  ;
        I_p1_rms = in[0]  ;

        noise = generateGaussianNoise(noise_mean, noise_sigma);
        I_p1_rms_n = I_p1_rms + noise;

        // primary side
        R_in = (V_p1_rms / I_p1_rms_n) * cos(theta);
        X_in = (V_p1_rms / I_p1_rms_n) * sin(theta);

        w_op = 1 / sqrt(L_p * C_p); // Primary angular freq
        w_os = 1 / sqrt(L_s * C_s); // Secondary angular freq

        //  Load resistance
        R_eq = - (((w * L_s - 1 / (w * C_s)) * (Rin - R_p)) /
                        (Xin - (w * L_p) + (1 / (w * C_p)))) - R_s;

        R_L = (pow(M_PI, 2)/8) * R_eq ;

        // Secondary
        numerator_Is1 = w * M * I_p1_rms_n;
```

```
        denominator_Is1 = sqrt(pow((R_s + R_eq), 2) +
                pow((w * L_s * (1 - pow(w_os, 2) / pow(w, 2))), 2));
        I_s1 = numerator_Is1 / denominator_Is1;

        // Output current
        I_o = (M_PI/ 2 * sqrt(2)) * I_s1;

        // Secondary vol
        V_s1 = I_s1 * R_eq;

        // Output voltage
        V_o = ((M_PI/ 2 * sqrt(2)) * V_s1 ;
        }
        }
        //
        out[0] = R_eq;
        out[1] = R_L;
        out[2] = V_o;
}

//////////////////////////////////////////////////////////////////////
// FUNCTION: SimulationBegin
// Initialization function. This function runs once at the beginning
// of simulation
// For parameter sweep or AC sweep simulation,
// this function runs at the beginning of each simulation cycle.
// Use this function to initialize static or global variables.
// const char *szId: (read only) Name of the C-block
// int nParameterCount: (read only)
// Ignore nParameterCount and pszParameters
// int *pnError: (write only)  assign  *pnError = 1;
//    strcpy(szErrorMsg, "Error message here...");
// DO NOT CHANGE THE NAME OR PARAMETERS OF THIS FUNCTION
void SimulationBegin(
const char *szId, int nInputCount, int nOutputCount,
int nParameterCount, const char ** pszParameters,
int *pnError, char * szErrorMsg,
void ** reserved_UserData, int reserved_ThreadIndex,
void * reserved_AppPtr)
{
        // ENTER INITIALIZATION CODE HERE...
}
//////////////////////////////////////////////////////////////////////
```

```
// FUNCTION: SimulationEnd
// Termination function. This function runs once at the end of
// simulation
// For parameter sweep or AC sweep simulation, this function
// runs at the end of each simulation cycle.
// Use this function to de-allocate any allocated memory or to save
// the result of simulation in an alternate file.
// Ignore all parameters for C-block
// DO NOT CHANGE THE NAME OR PARAMETERS OF THIS FUNCTION
void SimulationEnd(const char *szId, void ** reserved_UserData,
int reserved_ThreadIndex, void * reserved_AppPtr)
```

B. Kalman estimator code

```
// PSIM C block for Kalman_estimator

#include <stdlib.h>
#include <string.h>
#include <math.h>
#include <Psim.h>
#include <random>
#include <stdio.h>
#define M_PI 3.14159265358979323846
#define STATE_DIM 4
#define OUTPUT_DIM 1

// System parameters
static double Rp = 0.1474;
static double Rs = 0.1434;
static double Cp = 15.88e-9;
static double Cs = 16.30e-9;
static double Lp = 155.4e-6;
static double Ls = 155.56e-6;
static double M  = 41.547e-6;
static double Req = 1.0;
static double vp = 50.0;
double ip = 1.0;
static double f = 114000;
static double Ts = 1/f;
static double Iout = 1.0;
static double RL = 1.0;
static double Vout = 1.0;
```

```
// Noise(AWGN) parameters
static double noise_mean  = 0.0;
static double noise_sigma = 0.05;

// Kalman matrices
static double A[STATE_DIM][STATE_DIM];
static double B[STATE_DIM];
static double Cmat[OUTPUT_DIM][STATE_DIM] = {{1,0,0,0}};
static double P[STATE_DIM][STATE_DIM];
static double z[OUTPUT_DIM];
static double P0[STATE_DIM][STATE_DIM] =
{{0.5,0,0,0},{0,0.5,0,0},{0,0,0.5,0},{0,0,0,0.5}};
static double Q[STATE_DIM][STATE_DIM] =
{{0.03,0,0,0},{0,0.03,0,0},{0,0,0.03,0},{0,0,0,0.03}};
static double Rcov[OUTPUT_DIM][OUTPUT_DIM] = {{1e-8}};
static double Identity[STATE_DIM][STATE_DIM];
static double K[STATE_DIM][OUTPUT_DIM];
static double x_hat[STATE_DIM] = {1.0,1.0,1.0,1.0};

// counters
static int count = 0;
static int Ncount = 0;
static int flagSample = 1;
static double ts_kf = 8.77e-7;

double noise ;
double ip_noisy ;
// Box-muller transform
double generateGaussianNoise(double noise_mean, double noise_sigma) {
        static int haveSpare = 0;
        static double spare;
        double u, v, s;
        if (haveSpare) {
                haveSpare = 0;
                return noise_mean + noise_sigma * spare;
        }
        do {
                u = ((double)rand() / RAND_MAX) * 2.0 - 1.0;
                v = ((double)rand() / RAND_MAX) * 2.0 - 1.0;
                s = u*u + v*v;
        } while (s >= 1.0 || s == 0.0);
        s = sqrt(-2.0 * log(s) / s);
        spare = v * s;
```

```
        haveSpare = 1;
        return noise_mean + noise_sigma * (u * s);
}

void mat_identity(double M[STATE_DIM][STATE_DIM]) {
        int i, j;
        for (i = 0; i < STATE_DIM; i++) {
                for (j = 0; j < STATE_DIM; j++) {
                        M[i][j] = (i==j) ? 1.0 : 0.0;
                }
        }
}

void mat_copy(double dst[STATE_DIM][STATE_DIM],
double src[STATE_DIM][STATE_DIM]) {
        int i, j;
        for (i = 0; i < STATE_DIM; i++) {
                for (j = 0; j < STATE_DIM; j++) {
                        dst[i][j] = src[i][j];
                }
        }
}

// Kalman phases
void kalman_predict(double vp) {
        int i, j, k;
        double x_temp[STATE_DIM] = {0};
        for (i = 0; i < STATE_DIM; i++) {
                for (j = 0; j < STATE_DIM; j++) {
                        x_temp[i] += A[i][j] * x_hat[j];
                }
                x_temp[i] += B[i] * vp;
        }
        for (i = 0; i < STATE_DIM; i++) x_hat[i] = x_temp[i];

        double AP[STATE_DIM][STATE_DIM] = {{0}};
        double APA_T[STATE_DIM][STATE_DIM] = {{0}};
        for (i = 0; i < STATE_DIM; i++) {
                for (j = 0; j < STATE_DIM; j++) {
                        for (k = 0; k < STATE_DIM; k++) {
                                AP[i][j] += A[i][k] * P[k][j];
                        }
                }
```

```
        }
        for (i = 0; i < STATE_DIM; i++) {
                for (j = 0; j < STATE_DIM; j++) {
                        for (k = 0; k < STATE_DIM; k++) {
                                APA_T[i][j] += AP[i][k] * A[j][k];
                        }
                        P[i][j] = APA_T[i][j] + Q[i][j];
                }
        }
}

// Kalman measurement update
void kalman_update(double ip_noisy) {
        int i, j, k;
        double z_est = 0;
        for (i = 0; i < STATE_DIM; i++)
                z_est += Cmat[0][i] * x_hat[i];

        double innovation = ip_noisy - z_est;
        double S = Rcov[0][0];
        for (i = 0; i < STATE_DIM; i++) {
                for (j = 0; j < STATE_DIM; j++) {
                   S += Cmat[0][i] * P[i][j] * Cmat[0][j];
                }
        }
        for (i = 0; i < STATE_DIM; i++) {
                double sum = 0;
                for (j = 0; j < STATE_DIM; j++)
                        sum += P[i][j] * Cmat[0][j];
               K[i][0] = sum / S;
        }
        for (i = 0; i < STATE_DIM; i++)
                x_hat[i] += K[i][0] * innovation;

        double I_KC[STATE_DIM][STATE_DIM] = {{0}};
        double newP[STATE_DIM][STATE_DIM] = {{0}};
        for (i = 0; i < STATE_DIM; i++) {
                for (j = 0; j < STATE_DIM; j++) {
                   I_KC[i][j] = Identity[i][j] - K[i][0] * Cmat[0][j];
                }
        }
        for (i = 0; i < STATE_DIM; i++) {
                for (j = 0; j < STATE_DIM; j++) {
```

```
                    for (k = 0; k < STATE_DIM; k++) {
                        newP[i][j] += I_KC[i][k] * P[k][j];
                    }
                }
        }
        mat_copy(P, newP);
}

// initialize_kf, Discretize A and B matrix
void initialize_kf() {
        int i, j;
        double den = Lp * Ls - M * M;
        for (i = 0; i < STATE_DIM; i++) {
                for (j = 0; j < STATE_DIM; j++) {
                        A[i][j] = 0;
                }
        }
        A[0][0] = -(Rp * Ls) / den;
        A[0][1] =  (M * Rs) / den;
        A[0][2] = -Ls / den;
        A[0][3] =  M / den;
        A[1][0] =  (Rp * M) / den;
        A[1][1] = -(Lp * (Rs + Req)) / den;
        A[1][2] =  M / den;
        A[1][3] = -Lp / den;
        A[2][0] = 1.0 / Cp;
        A[3][1] = 1.0 / Cs;

        B[0] =  Ls / den;
        B[1] = -M / den;
        B[2] = 0;
        B[3] = 0;

        // Discretize  AA = I + ts_kf*A, BB = ts_kf*B
        for (i = 0; i < STATE_DIM; i++) {
                for (j = 0; j < STATE_DIM; j++) {
                        if (i == j) A[i][j] = 1.0 + A[i][j]*ts_kf;
                }
                B[i] *= ts_kf;
        }
        mat_identity(Identity);
        mat_copy(P, P0);
}
```

```
void SimulationBegin(const char* szId, int nIn, int nOut,
int nParam, const char** pszParam,
int* err, char* errMsg,
void** userData, int thIdx, void* appPtr) {
        srand(0);
        initialize_kf();
}

void SimulationStep(double t, double delt, double* in, double* out,
int* err, char* errMsg,
void** userData, int thIdx, void* appPtr) {
        int i;
        Ncount = Ts / delt;
        if (count >= Ncount) { flagSample = 1; count = 0; }
        if (flagSample) {
                flagSample = 0;
                Req = in[0];
                ip = in[1];

                noise = generateGaussianNoise(noise_mean, noise_sigma);
                ip_noisy = ip + noise;

                if (t >= 1e-3) {
                        kalman_predict(vp);
                        kalman_update(ip_noisy);
                }
                z = z_est ;
        }
        // estimates
        Iout = (M_PI/ 2 * sqrt(2) ) * z;
        Vout = (M_PI/ 2 * sqrt(2)) * z *Req;

        out[0] = Vout ;
        out[1] = Req;
        out[2] = Iout;
        ;
        count++;
}
void SimulationEnd(const char* szId, void** userData, int thIdx,
void* appPtr) {
        // cleanup
}
```

References

[1] S.-Y. R. Hui, Y. Yang, and C. Zhang, “Wireless power transfer: A paradigm shift for the next generation,” *IEEE Journal of Emerging and Selected Topics in Power Electronics*, vol. 11, no. 3, pp. 2412–2427, 2023.

[2] J. Park, J. Oh, Y. Bok, and I. Lee, “22 kw high-efficiency ipt system for wireless charging of electric vehicles,” *Journal of Power Electronics*, vol. 23, no. 2, pp. 374–386, 2023.

[3] Z. Zhang, H. Pang, A. Georgiadis, and C. Cecati, “Wireless power transfer–an overview,” *IEEE Transactions on Industrial Electronics*, vol. 66, no. 2, pp. 1044–1058, 2019.

[4] U. K. Madawala and D. J. Thrimawithana, “A single controller for inductive power transfer systems,” in *2009 35th Annual Conference of IEEE Industrial Electronics*, 2009, pp. 109–113.

[5] D. J. Thrimawithana and U. K. Madawala, “A primary side controller for inductive power transfer systems,” in *2010 IEEE International Conference on Industrial Technology*, 2010, pp. 661–666.

[6] M. Al-Greer, M. Armstrong, M. Ahmeid, and D. Giaouris, “Advances on system identication techniques for dc–dc switch mode power converter applications,” *IEEE Transactions on Power Electronics*, vol. 34, no. 7, pp. 6973–6990, 2019.

[7] A. Triviño-Cabrera, M. Ochoa, D. Fernández, and J. A. Aguado, "Independent primary-side controller applied to wireless chargers for electric vehicles," in *2014 IEEE International Electric Vehicle Conference (IEVC)*, 2014, pp. 1–5.

[8] H. Niu, G. Li, J. Lu, and X. Pan, "Parameter identification method with dynamic impedance modulation for the dwpt system," *IEEE Journal of Emerging and Selected Topics in Power Electronics*, vol. 10, no. 5, pp. 6332–6344, 2022.

[9] U. K. Madawala and D. J. Thrimawithana, "New technique for inductive power transfer using a single controller," *IET Power Electronics*, vol. 5, no. 2, pp. 248–256, 2012.

[10] J. P.-W. Chow, H. S.-H. Chung, and C.-S. Cheng, "Use of transmitter-side electrical information to estimate mutual inductance and regulate receiver-side power in wireless inductive link," *IEEE Transactions on Power Electronics*, vol. 31, no. 9, pp. 6079–6091, 2016.

[11] J. M. Miller, O. C. Onar, and M. Chinthavali, "Primary-side power flow control of wireless power transfer for electric vehicle charging," *IEEE Journal of Emerging and Selected Topics in Power Electronics*, vol. 3, no. 1, pp. 147–162, 2015.

[12] D. Li, P. Sun, K. Ji, Y. Liang, Y. Liu, and X. Wu, "Multi-mode switching and charging area division of multi-transmitter ipt system," *Journal of Power Electronics*, vol. 24, no. 7, pp. 1177–1188, 2024.

[13] Z. N. Low, R. A. Chinga, R. Tseng, and J. Lin, "Design and test of a high-power high-efficiency loosely coupled planar wireless power transfer system," *IEEE Transactions on Industrial Electronics*, vol. 56, no. 5, pp. 1801–1812, 2009.

[14] J. Hong, F. Pan, Z. Zhang, J. Teng, and D. He, “Constant current/voltage characteristics inductive power transfer system with variable static s-t/fc compensation,” *Journal of Power Electronics*, vol. 24, no. 3, pp. 480–491, 2024.

[15] M. Kato, T. Imura, and Y. Hori, “Study on maximize efficiency by secondary side control using dc-dc converter in wireless power transfer via magnetic resonant coupling,” *World Electric Vehicle Journal*, vol. 6, no. 4, pp. 858–862, 2013.

[16] K. Hata, T. Imura, and Y. Hori, “Dynamic wireless power transfer system for electric vehicles to simplify ground facilities - power control and efficiency maximization on the secondary side,” in *2016 IEEE Applied Power Electronics Conference and Exposition (APEC)*, 2016, pp. 1731–1736.

[17] A. Alkasir, S. E. Abdollahi, S. R. Abdollahi, and P. Wheeler, “Enhancement of dynamic wireless power transfer system by model predictive control,” *IET Power Electronics*, vol. 15, no. 1, pp. 67–79.

[18] X. Li, H. Wang, F. Zheng, X. Dai, Y. Sun, and A. P. Hu, “Wireless charging of substation inspection robots based on parameter estimation without communication,” *IEEE Transactions on Circuits and Systems II: Express Briefs*, vol. 71, no. 2, pp. 907–911, 2024.

[19] Y. Guo and Y. Zhang, “Secondary side voltage and current estimation of wireless power transfer systems,” *IEEE Transactions on Industry Applications*, vol. 58, no. 1, pp. 1222–1230, 2022.

[20] K. Song, Z. Li, Z. Du, G. Wei, and C. Zhu, “Design for constant output voltage and current controllability of primary side controlled wireless power transfer system,” in *2017*

IEEE PELS Workshop on Emerging Technologies: Wireless Power Transfer (WoW), 2017, pp. 1–6.

[21] J. Zeng, S. Chen, Y. Yang, and S. Y. R. Hui, “A primary-side method for ultrafast determination of mutual coupling coefficient in milliseconds for wireless power transfer systems,” *IEEE Transactions on Power Electronics*, vol. 37, no. 12, pp. 15 706–15 716, 2022.

[22] X. Li, L. Yang, Z. Xu, Y. Wu, S. Liu, and C. Cai, “A communication-free WPT system based on transmitter-side hybrid topology switching for battery charging applications,” *AIP Advances*, vol. 10, no. 4, p. 045302, 04 2020.

[23] O. Trachtenberg and A. Kuperman, “Output voltage and resistance assessment of load-independent-voltage-output frequency operating inductive wireless power transfer link utilizing input dc-side measurements only,” *Electronics*, vol. 10, no. 17, 2021.

[24] H. Zhu, B. Zhang, and L. Wu, “Output power stabilization for wireless power transfer system employing primary-side-only control,” *IEEE Access*, vol. 8, pp. 63 735–63 747, 2020.

[25] J. Zeng, J. Wu, K. Li, Y. Yang, and S. Y. R. Hui, “Dynamic monitoring of battery variables and mutual inductance for primary-side control of a wireless charging system,” *IEEE Transactions on Industrial Electronics*, vol. 71, no. 7, 2024.

[26] Y. Guo, Y. Zhang, S. Li, C. Tao, and L. Wang, “Load parameter joint identification of wireless power transfer system based on the dc input current and phase-shift angle,” *IEEE Transactions on Power Electronics*, vol. 35, no. 10, pp. 10 542–10 553, 2020.

[27] E. Chung, G. C. Lim, J.-I. Ha, and K. Y. Kim, "Output voltage control for series-series compensated wireless power transfer system without direct feedback from measurement or communication," in *2017 IEEE Energy Conversion Congress and Exposition (ECCE)*, 2017, pp. 4035–4040.

[28] K. Yue, Y. Liu, X. Zhang, M. Fu, J. Liang, and H. Wang, "Transmitter-side voltage-based mutual inductances and load tracking for two-transmitter lcc-s compensated wireless power transfer systems," *IEEE Journal of Emerging and Selected Topics in Power Electronics*, vol. 12, no. 2, pp. 2317–2332, 2024.

[29] J. Yin, D. Lin, C.-K. Lee, and S. Y. R. Hui, "A systematic approach for load monitoring and power control in wireless power transfer systems without any direct output measurement," *IEEE Transactions on Power Electronics*, vol. 30, no. 3, pp. 1657–1667, 2015.

[30] C. Liu, W. Han, Y. Hu, and B. Zhang, "Simultaneous identification of multiple parameters in wireless power transfer systems using primary variable capacitors," *Applied Sciences*, vol. 14, no. 2, 2024.

[31] J. Liu, G. Wang, G. Xu, J. Peng, and H. Jiang, "A parameter identification approach with primary-side measurement for dc–dc wireless-power-transfer converters with different resonant tank topologies," *IEEE Transactions on Transportation Electrification*, vol. 7, no. 3, pp. 1219–1235, 2021.

[32] K. Song, Z. Li, J. Jiang, and C. Zhu, "Constant current/voltage charging operation for series–series and series–parallel compensated wireless power transfer systems employing

primary-side controller," *IEEE Transactions on Power Electronics*, vol. 33, no. 9, pp. 8065–8080, 2018.

[33] Z. Li, G. Wei, S. Dong, K. Song, and C. Zhu, "Constant current/voltage charging for the inductor–capacitor–inductor-series compensated wireless power transfer systems using primary-side electrical information," *IET Power Electronics*, vol. 11, no. 14, pp. 2302–2310.

[34] R. Dai, W. Zhou, Y. Chen, Z. Zhu, and R. Mai, "Pulse density modulation based mutual inductance and load resistance identification method for wireless power transfer system," *IEEE Transactions on Power Electronics*, vol. 37, no. 8, pp. 9933–9943, 2022.

[35] Y.-G. Su, L. Chen, X.-Y. Wu, A. P. Hu, C.-S. Tang, and X. Dai, "Load and mutual inductance identification from the primary side of inductive power transfer system with parallel-tuned secondary power pickup," *IEEE Transactions on Power Electronics*, vol. 33, no. 11, pp. 9952–9962, 2018.

[36] J. Zeng, Y. Yang, K. Li, S. Chen, and S. Y. R. Hui, "An ultrafast estimation method for coupling coefficient and receiver resonant frequency in universal wireless power transfer systems," *IEEE Transactions on Power Electronics*, vol. 39, no. 4, pp. 4870–4883, 2024.

[37] Y. Yang, S. C. Tan, and S. Y. R. Hui, "Fast hardware approach to determining mutual coupling of series–series-compensated wireless power transfer systems with active rectifiers," *IEEE Transactions on Power Electronics*, vol. 35, no. 10, pp. 11 026–11 038, 2020.

[38] J. Yin, D. Lin, C. K. Lee, T. Parisini, and S. Y. Hui, "Front-end monitoring of multiple loads in wireless power transfer systems without wireless communication systems," *IEEE Transactions on Power Electronics*, vol. 31, no. 3, pp. 2510–2517, 2016.

[39] W. Xiao, R. Shen, B. Zhang, D. Qiu, Y. Chen, and F. Xie, "Multiple parameters estimation based on transmitter side information in wireless power transfer system," *IEEE Access*, vol. 7, pp. 164 835–164 843, 2019.

[40] J. Yin, D. Lin, T. Parisini, and S. Y. Hui, "Front-end monitoring of the mutual inductance and load resistance in a series–series compensated wireless power transfer system," *IEEE Transactions on Power Electronics*, vol. 31, no. 10, pp. 7339–7352, 2016.

[41] Y. Liu, U. K. Madawala, R. Mai, and Z. He, "Primary-side parameter estimation method for bidirectional inductive power transfer systems," *IEEE Transactions on Power Electronics*, vol. 36, no. 1, pp. 68–72, 2021.

[42] L. Wang, P. Sun, Y. Liang, L. He, X. Wu, and Q. Deng, "Research on the control strategy of communication-free ipt system based on multiparameter joint real-time identification," *IEEE Transactions on Power Electronics*, vol. 39, no. 1, pp. 1912–1926, 2024.

[43] Y.-G. Su, H.-Y. Zhang, Z.-H. Wang, A. Patrick Hu, L. Chen, and Y. Sun, "Steady-state load identification method of inductive power transfer system based on switching capacitors," *IEEE Transactions on Power Electronics*, vol. 30, no. 11, pp. 6349–6355, 2015.

[44] Z. Liu, L. Wang, Y. Guo, and S. Li, "Primary-side linear control for constant current/voltage charging of the wireless power transfer system based on the lcc-n com-

pensation topology," *IEEE Transactions on Industrial Electronics*, vol. 69, no. 9, pp. 8895–8904, 2022.

[45] S. Li, L. Wang, Y. Guo, and Z. Liu, "Flexible energy-transfer control of dynamic wireless power transfer system based on estimation of load and mutual inductance," *IEEE Transactions on Industry Applications*, vol. 58, no. 1, pp. 1157–1167, 2022.

[46] X. Sheng and L. Shi, "Mutual inductance and load identification method for inductively coupled power transfer system based on auxiliary inverter," *IEEE Transactions on Vehicular Technology*, vol. 69, no. 2, pp. 1533–1541, 2020.

[47] J. Zeng, S. Chen, K. Li, and S. Y. R. Hui, "A front-end monitoring method for coupling coefficient and receiver resonant frequency in the ss-compensated wireless power transfer systems with unknown receiver parameters," *IEEE Transactions on Power Electronics*, vol. 39, no. 5, pp. 6466–6476, 2024.

[48] Z. Li, H. Liu, Y. Tian, and Y. Liu, "Constant current/voltage charging for primary-side controlled wireless charging system without using dual-side communication," *IEEE Transactions on Power Electronics*, vol. 36, no. 12, 2021.

[49] Y. Yang, J. Zeng, and S. Y. R. Hui, "A fast primary-side current and voltage control for direct wireless battery chargers," *IEEE Journal of Emerging and Selected Topics in Power Electronics*, vol. 12, no. 1, pp. 355–366, 2024.

[50] Y. Zhang, S. Chen, X. Li, and Y. Tang, "Dual-side phase-shift control of wireless power transfer implemented on primary side based on driving windings," *IEEE Transactions on Industrial Electronics*, vol. 68, no. 9, pp. 8999–9002, 2021.

[51] Y. Mao, Y. Yang, and K. Wang, "A primary-side fixed-frequency cc and cv output control for single-stage wireless battery chargers with series compensation receivers," *IEEE Transactions on Transportation Electrification*, vol. 10, no. 2, pp. 3407–3415, 2024.

[52] Y. Wei and F. Wu, "Indirect control strategy of secondary current for lcc-series compensated wireless power transfer system based on primary current closed-loop control," *IEEE Transactions on Transportation Electrification*, vol. 8, no. 2, pp. 1553–1565, 2022.

[53] L. Wang, P. Sun, Y. Liang, J. Sun, X. Wu, H. Shen, and Q. Deng, "Joint real-time identification for mutual inductance and load charging parameters of ipt system," *IEEE Journal of Emerging and Selected Topics in Power Electronics*, vol. 11, no. 4, pp. 4574–4590, 2023.

[54] D. Yang, S. Won, J. Tian, Z. Cheng, and J. Kim, "A method of estimating mutual inductance and load resistance using harmonic components in wireless power transfer system," *Energies*, vol. 12, no. 14, 2019.

[55] K. Chen, Z. Nie, C. Yan, N. C. Cheung, E. K.-W. Cheng, and J. Pan, "A noncommunication mutual inductance estimation method for multiple transmitters ss-compensated dynamic wireless power transfer with low calculation effort," *IEEE Transactions on Power Electronics*, vol. 39, no. 7, pp. 7803–7807, 2024.

[56] Y. Guo, Y. Zhang, W. Zhang, and L. Wang, "Battery parameter identification based on wireless power transfer system with rectifier load," *IEEE Transactions on Industrial Electronics*, vol. 68, no. 8, pp. 6893–6904, 2021.

[57] E. G. Marques, A. M. S. Mendes, M. S. Perdigão, and V. S. Costa, "Design methodology of a three coil ipt system with parameters identification for evs," *IEEE Transactions on Vehicular Technology*, vol. 70, no. 8, pp. 7509–7521, 2021.

[58] J. P.-W. Chow, H.-H. Chung, C.-S. Cheng, and W. Wang, "Use of transmitter-side electrical information to estimate system parameters of wireless inductive links," *IEEE Transactions on Power Electronics*, vol. 32, no. 9, pp. 7169–7186, 2017.

[59] Z.-H. Wang, Y.-P. Li, Y. Sun, C.-S. Tang, and X. Lv, "Load detection model of voltage-fed inductive power transfer system," *IEEE Transactions on Power Electronics*, vol. 28, no. 11, pp. 5233–5243, 2013.

[60] W. Hong, S. Lee, E. Choi, and S.-H. Lee, "Observer-based maximum efficiency point tracking controller for a series–series tuned, 60 khz inductive power transfer system," *IEEE Transactions on Transportation Electrification*, vol. 10, no. 3, pp. 5334–5343, 2024.

[61] S. A. Khan and D. Ahn, "Coupling estimation and maximum efficiency tracking in multi-transmitters wpt for fast moving receiver," *IEEE Access*, vol. 12, pp. 9952–9962, 2024.

[62] F. Xu, S.-C. Wong, and C. K. Tse, "Inductive power transfer system with maximum efficiency tracking control and real-time mutual inductance estimation," *IEEE Transactions on Power Electronics*, vol. 37, no. 5, pp. 6156–6167, 2022.

[63] X. Li, D. Zhou, S. Jia, X. Liu, and J. Zou, "A wpt system with wide-range voltage gains and soft switching via primary-side hybrid modulation," *IEEE Transactions on Power Electronics*, vol. 39, no. 7, pp. 8985–8997, 2024.

[64] Wireless Power Consortium (WPC), "The qi wireless power transfer system – power class 0 specification," *IEEE Access*, vol. 1.2.4, no. 4, 2018.

[65] S. Y. Hui, "Planar wireless charging technology for portable electronic products and qi," *Proceedings of the IEEE*, vol. 101, no. 6, pp. 1290–1301, 2013.

[66] D. Simon, *Optimal State Estimation: Kalman, H Infinity, and Nonlinear Approaches*, 1st ed. Hoboken, NJ: Wiley-Interscience, 2006.

[67] Q. Li, R. Li, K. Ji, and W. Dai, "Kalman filter and its application," in *2015 8th International Conference on Intelligent Networks and Intelligent Systems (ICINIS)*, 2015, pp. 74–77.

[68] Texas Instruments, "Tms320f2837xd dual-core real-time microcontrollers," dallas, TX, USA, TMS320F28379D datasheet, Feb. 2024. Accessed: Aug, 2025. [Online]. Available: https://www.ti.com/product/TMS320F28379D.

[69] Altair, "Power electronics and motor drive software | altair® psim™," accessed: Aug. 2025. [Online]. Available: https://altair.com/psim-applications.

[70] D. W. Scott, "Box–muller transformation," *WIREs Computational Statistics*, vol. 3, no. 2, pp. 177–179, mar 2011. [Online]. Available: https://doi.org/10.1002/wics.148

[71] Texas Instruments, "Dac7554idgs — low-power, low-glitch, 12-bit dac (vssop-10)," dallas, TX, USA, DAC7554IDGS datasheet, Accessed: Aug. 2025. [Online]. Available: https://www.ti.com/product/DAC7554/part-details/DAC7554IDGS.

[72] TexasInstruments, “Tlv2352 dual low-voltage differential comparators,” dallas, TX, USA, TLV2352 datasheet, Jul. 2025. Accessed: Nov, 2025. [Online]. Available: https://www.ti.com/product/TLV2352.

[73] J. Zeng, Y. Yang, K. Li, S. Chen, and S. Y. R. Hui, “An ultrafast estimation method for coupling coefficient and receiver resonant frequency in universal wireless power transfer systems,” *IEEE Transactions on Power Electronics*, vol. 39, no. 4, pp. 4870–4883, 2023.

[74] R. Dai, W. Zhou, Y. Chen, Z. Zhu, and R. Mai, “Pulse density modulation based mutual inductance and load resistance identification method for wireless power transfer system,” *IEEE Transactions on Power Electronics*, vol. 37, no. 8, pp. 9933–9943, 2022.

[75] S. Lee and S.-H. Lee, “Observer-based online parameter identification of series–series tuned inductive power transfer system,” *IEEE Transactions on Industrial Electronics*, vol. 72, no. 3, pp. 2927–2937, 2025.